CHAPTER 4

Comparison of Photocatalytic Properties of Composited Bismuth Vanadate with Titanium Dioxide, Tungsten Trioxide and Cerium Dioxide

4.1 Introduction

Bismuth vanadate ($BiVO_4$) has been attracted more attention in recent years especially in the field of photocatalysis due to its narrow band gap energy of 2.4 eV, which allows to be activated by visible-light irradiation [1]. Thus, it has been used in the photocatalytic degradation of organic dyes in aqueous solution and splitting of water for oxygen evolution under sunlight irradiation [1–4]. However, one of limitations of the photocatalytic efficiency in pure $BiVO_4$ is the fast recombination of photogenerated electrons and holes [4, 5]. In order to enhance the photocatalytic activity of $BiVO_4$, the essential requirement is to fabricate an electronic barrier of the photocatalysts, which contribute to the separation of the photogenerated electrons and holes. These charge separations prevent the electrons and holes from recombination. Thus, the electrons and holes have more opportunities to participate in reduction and oxidation reactions for the degradation of the organic dye on their surface [4–6]. Many attempts have been performed, such as doping these semiconductors with metal and nonmetals and sensitizing composite with other metal oxide semiconductors [4, 7, 8]. Thus, the coupling $BiVO_4$ with different metal oxides (TiO_2, CeO_2 and WO_3) was studied in this work.

Recently, some publications of coupled $BiVO_4$ with other metal oxides such as $BiVO_4/Bi_2O_3$ [9, 10], $V_2O_5/BiVO_4$ [11, 12], $BiVO_4/TiO_2$ [13–15], $BiVO_4/WO_3$ [6, 16–19], $BiVO_4/CdS$ [19], $BiVO_4/CuCr_2O_4$ [20] and $BiVO_4/CuWO_4$ [21] have been reported in water purification and water spitting applications. Li *et al.* [9] reported that $Bi_2O_3/BiVO_4$ sub-micrometer sphere composite was sythesized by two steps processes of a simple decomposition reaction for monoclinic Bi_2O_3 at 600ºC for 6 h, and homogeneous precipitation method at room temperature for tetragonal $BiVO_4$. There is another report on the synthesis of the porous peanut-like $Bi_2O_3/BiVO_4$ composite with heterojunctions synthesized by a one-step mixed solvothermal method with the assistance of a L-lysine template [10]. They also investigated the photocatalytic degradation of organic dyes (rhodamine B and methylene blue), and the composite catalysts exhibited higher photocatalytic activities.

Jiang *et al.* [11] reported that $V_2O_5/BiVO_4$ composite photocatalysts with orthorhombic and monoclinic structures of V_2O_5 and $BiVO_4$, respectively were synthesizd by a one-step solution combustion synthesis method. The 9 mol% $V_2O_5/BiVO_4$ composite photocatalyst annealed at 500ºC for 4 h exhibited the best photocatalytic degradation activities of methylene blue.

Hu *et al.* [14] reported that the $BiVO_4/TiO_2$ heterostructure was synthesized by a sol-gel method with optimum content of $BiVO_4:TiO_2$ as 1:200 (mass ratio), which could enhanced photocatalytic degradation of benzene under visible light irradiation. Zhang *et al.* [15] also synthesized $BiVO_4/TiO_2$ composite photocatalysts with heterojunction structures of monoclinic $BiVO_4$ and anatase TiO_2 by a one-step of combined microwave and hydrothermal method at 200ºC for 30 min, and the 20%$TiO_2/BiVO_4$ showed the best photocatalytic activity for degradation of Rhodamine B.

Furthermore, Chatchai *et al.* [16] studied the photocatalytic and photoelectrocatalytic properties of $WO_3/BiVO_4$ photoanode for degradation of methylene blue, which the composite electrode was fabricated by electrodeposition technique. The photo-electrocatalytic system of $WO_3/BiVO_4$ photoanode with Cu_2O photocathode modified with Ag showed higher performance for methylene blue degradation under visible light irradiation than the individual photocatalytic system.

For all photocatalytic degradation of organic pollutants of the above composites, it could be similarly observed that the composite semiconductor photocatalysts were more photocatalytically active than its individual catalysts. Thus, the possible mechanisms of the coupled $BiVO_4/TiO_2$, $BiVO_4/CeO_2$ and $BiVO_4/WO_3$ systems for degradation of MB dye in aqueous solution under visible light irradiation were also studied in this research. Moreover, X-ray photoelectron spectroscopy (XPS) and Transmission electron microscopy (TEM) were also employed to characterize these composite photocatalysts.

4.2 Experimental section

4.2.1 Chemicals

The chemicals was used for synthesizing pure $BiVO_4$, TiO_2 and $BiVO_4/TiO_2$ composites by a coupling of precipitation and sol-gel methods, and WO_3 and $BiVO_4/WO_3$ composites by precipitation method are as shown in Table 4.1.

Table 4.1 Chemicals for synthesis of pure $BiVO_4$, WO_3, TiO_2, $BiVO_4/WO_3$ and $BiVO_4/TiO_2$ composites.

Chemicals	Purity	Molecular formula	Molecular Weight (g/mol)	Company
Ammonium hydroxide	25.0 wt.% in water	NH_4OH	17.00	Merck
Ammonium metavanadate	99.9%	NH_4VO_3	116.98	Aldrich
Bismuth (III)nitrate pentahydrate	98.0%	$Bi(NO_3)_3.5H_2O$	485.07	Sigma-Aldrich
Citric acid	99.0%	$C_6H_8O_7$	192.12	Ajax
Ethanol absolute	100%	C_2H_5OH	46.08	Ajax
Ethylene glycol	99.5%	$C_2H_6O_2$	62.07	Fluka
Hydrochloric acid	37.0 wt.% in water	HCl	36.46	Merck
Nitric acid	70.0 wt.% in water	HNO_3	63.01	Ajax
Sodium tungstate (VI)dihydrate	99.0%	$Na_2WO_4.\ 2H_2O$	329.85	Sigma-Aldrich
Titanium(IV) isopropoxide	97.0%	$C_{12}H_{28}O_4Ti$	284.22	Sigma-Aldrich

4.2.2 Equipment

The synthesized TiO_2, WO_3, $BiVO_4$, $BiVO_4/TiO_2$ and $BiVO_4/WO_3$ composite powders and films were characterized using the equipment as the following list.

- Brunauer-Emmett-Teller (BET) analysis (Autosorb 1 MP, Quantachrome)
- Profilometer (Dektak 150, Veeco)
- Raman spectroscopy (JOBIN YVON, HORIBA)
- Scanning electron microscope (JSM-7500FA, JEOL)
- Transmission electron microscope (JSM-2010, JEOL)
- UV-Vis spectrophotometer (UV-3600, Shimadzu) with an integrating sphere attachment (ISR-3100, Shimadzu).
- UV-Vis spectrophotometer (8453 UV-Vis Diode Array System, Agilent Technologies)
- X-ray diffraction spectrometer (Philip X’ Pert PRO PW 3719)
- X-ray photoelectron spectroscope (AXIS Ultra DLD, Kratos Analytical)
- Visible-light source (50 W, SOLUX Halogen lamp, with a 400 nm cut off filter).

4.2.3 Synthesis of $BiVO_4/TiO_2$ composites

$BiVO_4/TiO_2$ nanocomposite catalysts with different mole ratios between $BiVO_4$ and TiO_2 were synthesized by coupling a homogeneous precipitation and sol-gel methods [22, 23]. First, pure $BiVO_4$ powder was synthesized by the homogeneous precipitation method as previously described in Chapter 2. The sol-gel method reported by Wetchakun *et al.* [23] was used for the synthesis of pure TiO_2 and the $BiVO_4/TiO_2$ nanocomposite with different mole ratios. Typically, 20 mL titanium tetraisopropoxide (TTIP) was dissolved in 250 mL 6 M nitric acid solution and mixed until a homogeneous solution was obtained. The mixture of TTIP and nitric acid solution was put into a cellophane membrane and then placed in solution containing a 1:1 v/v ratio (350 mL) of absolute ethanol and deionized water with 0.5−1%concentrated (25%) ammonia. Then, the as-synthesized $BiVO_4$ powder with different amount of mole ratios was subsequently added to the above mixture in the cellophane pouch to synthesize $BiVO_4/TiO_2$ composite powders. The mixture inside the cellophane pouch was kept stirring with magnetic stirrer bar and heated temperature at 80°C for 1 h. After the completion of the dialysis process, the suspension was centrifuged at 5000 rpm for 10 min, washed with deionized water and then dried in an oven at 60°C for 24 h. The obtained powder was finally calcined in a furnace at the temperature in the range of 450ºC for 2 h. For control experiments, pure TiO_2 photocatalyst was also synthesized by the procedure described above.

4.2.4 Synthesis of $BiVO_4/WO_3$ composites

$BiVO_4/WO_3$ nanocomposite catalysts with different mole ratios between $BiVO_4$ [22] and WO_3 were synthesized by precipitation method. Firstly, pure WO_3 powder was synthesized by dissolving 5 g of sodium tungstate dihydrate ($Na_2WO_4.2H_2O$) in solution containing 10 g of citric acid, 75 mL of ethylene glycol and 25 mL of deionized water under continuous stirring. The solution was heated at 70ºC, and then 25 mL of 1M hydrochloric acid (HCl) was added to the above solution (pH as approximately 1). The mixed solution was kept under continuous stirring and maintaining a constant temperature until the formation of a yellow-green precipitate. Finally, the powder was separated by centrifugation, washed with deionized water and ethanol several times, dried at 60ºC for 24 h, and then calcined at 450ºC for 1 h. The co-precipitation method for synthesis of the pure $BiVO_4$ as discussed in Chapter 2 was used to synthesize $BiVO_4/WO_3$ composite powders with different mole ratios. One difference, the WO_3 powder with different mole ratios was put in the mixed precursors before adjusting pH with ammonium hydroxide. The $BiVO_4/WO_3$ composite powders were calcined again at 450ºC for 1 h to remove ethylene glycol after washing with deionized water and drying overnight at 60ºC.

Furthermore, all synthesized catalysts in film forms were fabricated by doctor blading on glass substrates and their photocatalytic activities were also investigated by degradation of methylene blue in aqueous solution as an organic pollutant model under visible light irradiation with the same experimental as previously described in Chapter 2 [24, 25]. For thicknesses of all fabricated films in this research were controlled to be about 2 μm as discussed previously in Chapter 3 the effect of film thicknesses to photocatalytic activities. The films were measured by using a profilometer (Veeco Dektak 150). Photographs of the as-prepared $BiVO_4/TiO_2$ composite films and the as-prepared $BiVO_4/WO_3$ composite films with different mole ratios are illuminated in Figure 4.1 and Figure 4.2, respectively.

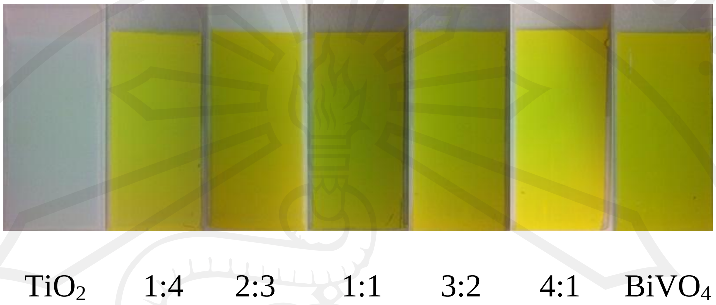

Figure 4.1 Photographs of TiO_2, 1:4$BiVO_4/TiO_2$, 3:2$BiVO_4/TiO_2$, 1:1$BiVO_4/TiO_2$, 2:3$BiVO_4/TiO_2$, 4:1$BiVO_4/TiO_2$ composite and $BiVO_4$ films on plain glass substrates after annealing at 500°C for 1 h.

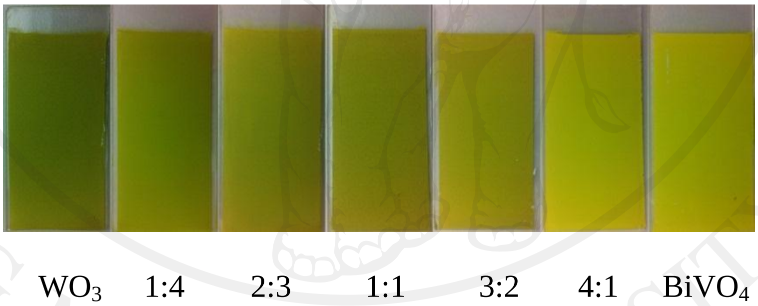

Figure 4.2 Photographs of WO_3, 1:4$BiVO_4/WO_3$, 3:2$BiVO_4/WO_3$, 1:1$BiVO_4/WO_3$, 2:3$BiVO_4/WO_3$, 4:1$BiVO_4/WO_3$ composite and $BiVO_4$ films on plain glass substrates after annealing at 500°C for 1 h.

4.3 Results and discussion for $BiVO_4/TiO_2$ composites

4.3.1 Characterization of $BiVO_4/TiO_2$ composite powders

The phase transition and crystallinity of the $BiVO_4/TiO_2$ composite powders synthesized by the coupled precipitation and sol-gel methods with different ratio of $BiVO_4$:TiO_2 were analyzed by X-ray diffraction (a Philip X' Pert

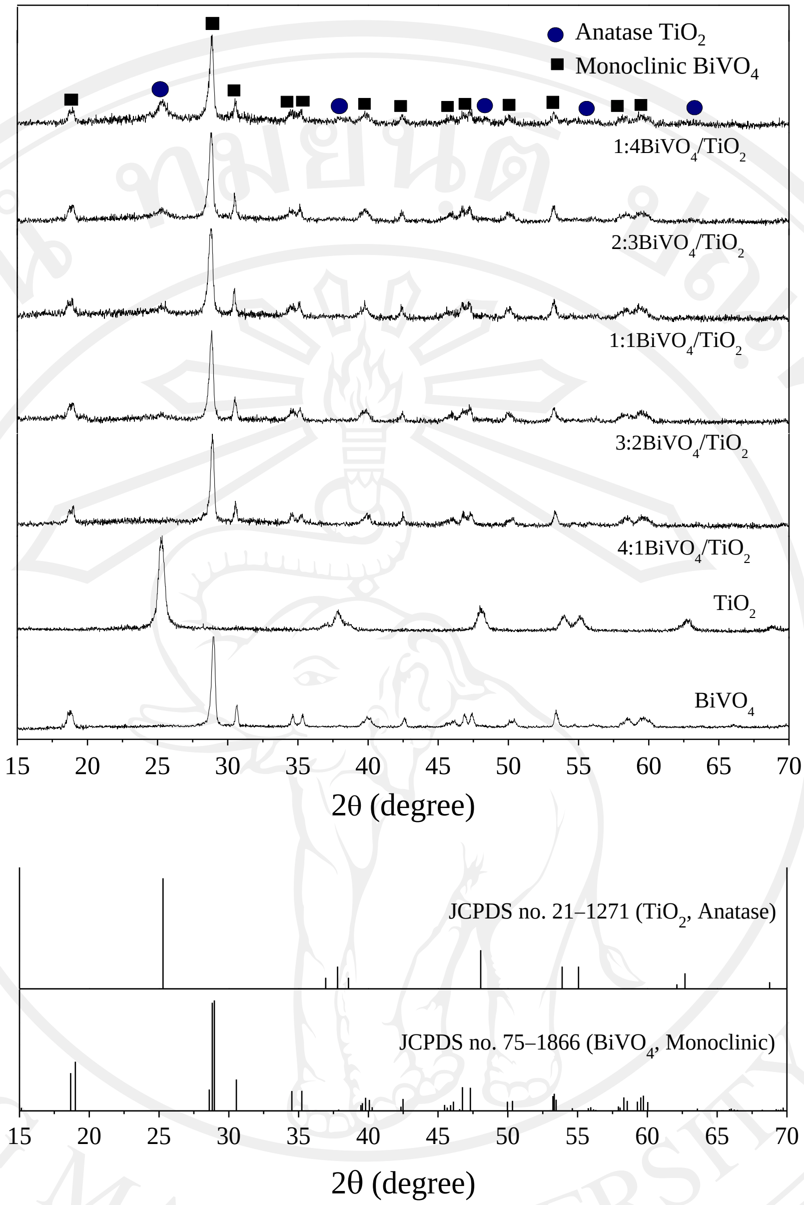

Figure 4.3 XRD patterns of pure $BiVO_4$ powder, pure TiO_2 powder and $BiVO_4$/TiO_2 composite powder with different mole ratios.

PRO PW 3719 XRD) using CuKα radiation (λ = 0.154 nm) at 2θ = 15−70° with a step size of 0.06° and a scanning speed of 0.72°/min. Figure 4.3 shows the XRD patterns of pure $BiVO_4$, TiO_2 and $BiVO_4$/TiO_2 composite powders with mole ratios of 4:1, 3:2, 1:1, 2:3 and 1:4. For the XRD pattern of pure $BiVO_4$ powder, all peaks could be confirmed to be the monoclinic phase of $BiVO_4$, which matched well with the JCPDS file no. 75−1866 and the diffraction peaks correspond to monoclinic $BiVO_4$ phase are at 2θ =

28.8°, 30.55°, 34.5°, 35.2°, 39.8°, and 42.5°. On the other hand, matching the XRD patterns of pure TiO_2 powder could be identified as the JCPDS file no. 21−1272, and the diffraction peaks correspond to tetragonal TiO_2 (anatase) are at $2\theta = 25.3°, 37.8°, 48.0°, 53.9°, 55.0°$ and 62.7°. In XRD patterns of composite powders, it was obviously seen that the XRD patterns of the $BiVO_4/TiO_2$ composites with 3:2, 1:1, 2:3 and 1:4 mole ratios showed the formation of two phases of monoclinic $BiVO_4$ and tetragonal TiO_2, $BiVO_4$ as a major phase with higher crystallinity and TiO_2 as a minor phase, and the TiO_2 phase increased with increasing amount of TiO_2 ratio. Furthermore, the TiO_2 phase was not appeared in the $BiVO_4/TiO_2$ composite with 4:1 mole ratio, which was possibly because that the amount of TiO_2 was too low, the size of TiO_2 particles was too small and the crystallinity of the $BiVO_4$ phase was high affecting to TiO_2 peaks nonappearance.

Table 4.2 Comparison of phase composition and crystalline size of $BiVO_4/TiO_2$ composite powders with different mole ratios.

Samples	**Phase composition (%)**		**Crystalline size (nm)**	
	$BiVO_4$	**TiO_2**	**$BiVO_4$**	**TiO_2**
$BiVO_4$	100	-	18.84	-
4:1$BiVO_4/TiO_2$	100	-	16.65	-
3:2$BiVO_4/TiO_2$	95.05	4.95	17.15	9.85
1:1$BiVO_4/TiO_2$	91.86	8.14	16.65	7.02
2:3$BiVO_4/TiO_2$	87.46	12.54	16.65	5.97
1:4$BiVO_4/TiO_2$	80.47	19.53	14.15	6.61
TiO_2	-	100	-	9.06

The percentage of the tetragonal TiO_2 phase could be calculated by the normalised ratios of relative intensities for the (101) peak of tetragonal TiO_2 and (200) peak of monoclinic $BiVO_4$, as shown in Equation (3.1) in Chapter 3, and the averagecrystalline sizes of $BiVO_4$ and TiO_2 particles in the composites were also estimated from the Scherrer equation as shown in Equation (3.2) in Chapter 3.

The summarized phase compositions and crystalline sizes of the $BiVO_4/TiO_2$ composite powders with different mole ratios are shown in Table 4.2. It was found that $BiVO_4$ in the $BiVO_4/TiO_2$ composite had higher crystallinity even loading with similar or lower ratios (1:1, 2:3 and 1:4 $BiVO_4/TiO_2$ composite), and crystalline size of $BiVO_4$ was observed to be bigger than TiO_2. Furthermore, Figure 4.3 clearly revealed that the intensity of the crystalline $BiVO_4$ gradually decreased with increasing of the amount of TiO_2 ratio, possibly because the TiO_2 nanoparticles were more covered on the surface of the $BiVO_4$ particle in the $BiVO_4/TiO_2$ composite.

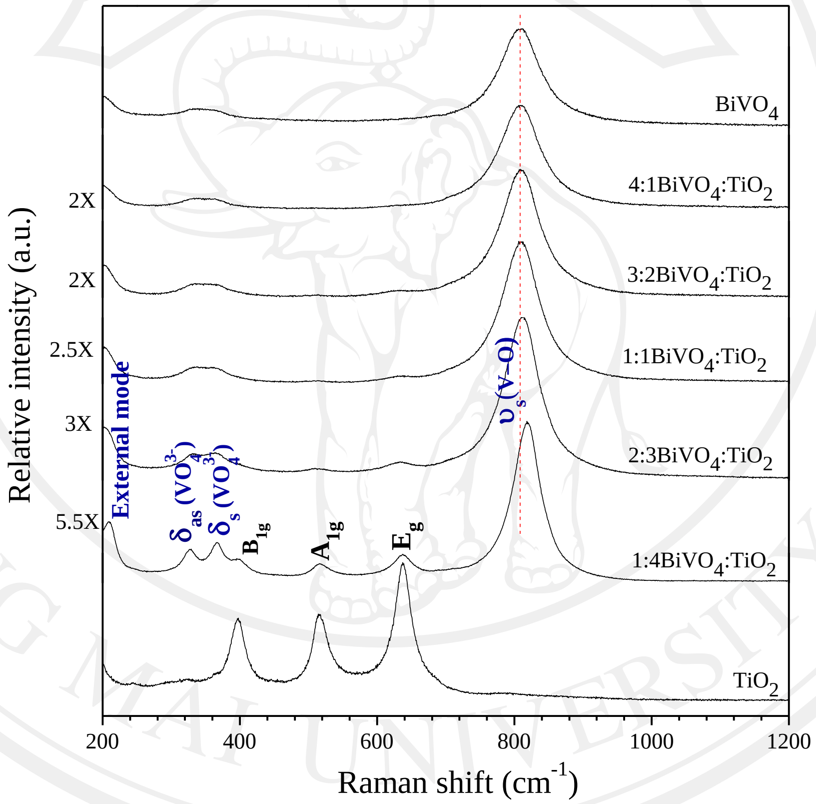

Figure 4.4 Raman spectra of pure $BiVO_4$, pure TiO_2 and $BiVO_4/TiO_2$ composite powder with different mole ratios.

The Raman spectra for the $BiVO_4/TiO_2$ and bare TiO_2 photocatalyst are shown in Figure 4.4. The characteristic spectra of the pure TiO_2 powder at 398.2 (B_{1g}), 516.5 (A_{1g}), 634.1 cm^{-1} (E_g) were attributed to the Raman active bands of the anatase TiO_2, similar to the results reported by Miao *et al.* [26] and Xue *et al.* [27]. For the pure $BiVO_4$ powder, Raman spectra at 208.7, 331.9, 357.7 and 808.9 cm^{-1} were observed, which are typical vibrational bands of monoclinic $BiVO_4$ (the label in Figure 4.4) in agreeing well with the reported works by Gotić *et al.* [28] and Zhang *et al.* [29]. The two Raman spectra at 331.9 and 357.7 cm^{-1} were assigned to the asymmetric and the asymmetric and symmetric bending vibrations of VO_4^{3-} tetrahedron, respectively. The Raman peak at 808.9 cm^{-1} corresponded to the symmetric V–O stretching mode.

Additionally, the Raman spectrum at lower wave number at 208.7 cm^{-1} was assigned to external vibration modes. For the $BiVO_4/TiO_2$ composites, characteristic Raman spectra for both $BiVO_4$ and TiO_2 were found in 2:3 and 1:4 $BiVO_4/TiO_2$ composites, and the peak intensities belonged to TiO_2 were increased when the mole ratio of TiO_2 to $BiVO_4$ increased. This could be attributed to a lower coverage of TiO_2 particles on the $BiVO_4$ surface. Appealingly, the dominated and strong spectrum of the $BiVO_4/TiO_2$ composites at 810.5 cm^{-1} was gradually shifted to higher wavelength comparing to the pure $BiVO_4$, and their spectrum intensities were obviously decreased when increasing the mole ratio of $BiVO_4$. This could possibly suggest that it was not the simple metal oxide mixture but the chemical interaction between the monoclinic $BiVO_4$ and the anatase TiO_2 existing in the composites, clearly seen in the 1:4$BiVO_4/TiO_2$ composite, leading to the decrease of the symmetry of the anatase TiO_2 molecules [30, 31].

In order to confirm the composition of the $BiVO_4/TiO_2$ composite and to take a more detailed look at the interactions between TiO_2 and $BiVO_4$ particles, the 1:1$BiVO_4/TiO_2$ composite was also characterized by XPS and compared with pure TiO_2 and $BiVO_4$. As shown in Figure 4.5, the XPS spectra of the (a) survey, (b) Bi 4f, V 2p, Ti 2p and 1s regions for the 1:1$BiVO_4/TiO_2$ composite compared to pure TiO_2 and $BiVO_4$. Figure 4.5(a) represents typical XPS survey spectra for the TiO_2, $BiVO_4$ and 1:1$BiVO_4/TiO_2$ composite. As expected in the composite catalysts the spectrum displayed the peaks of Bi, V, O, Ti and C. The binding energy of

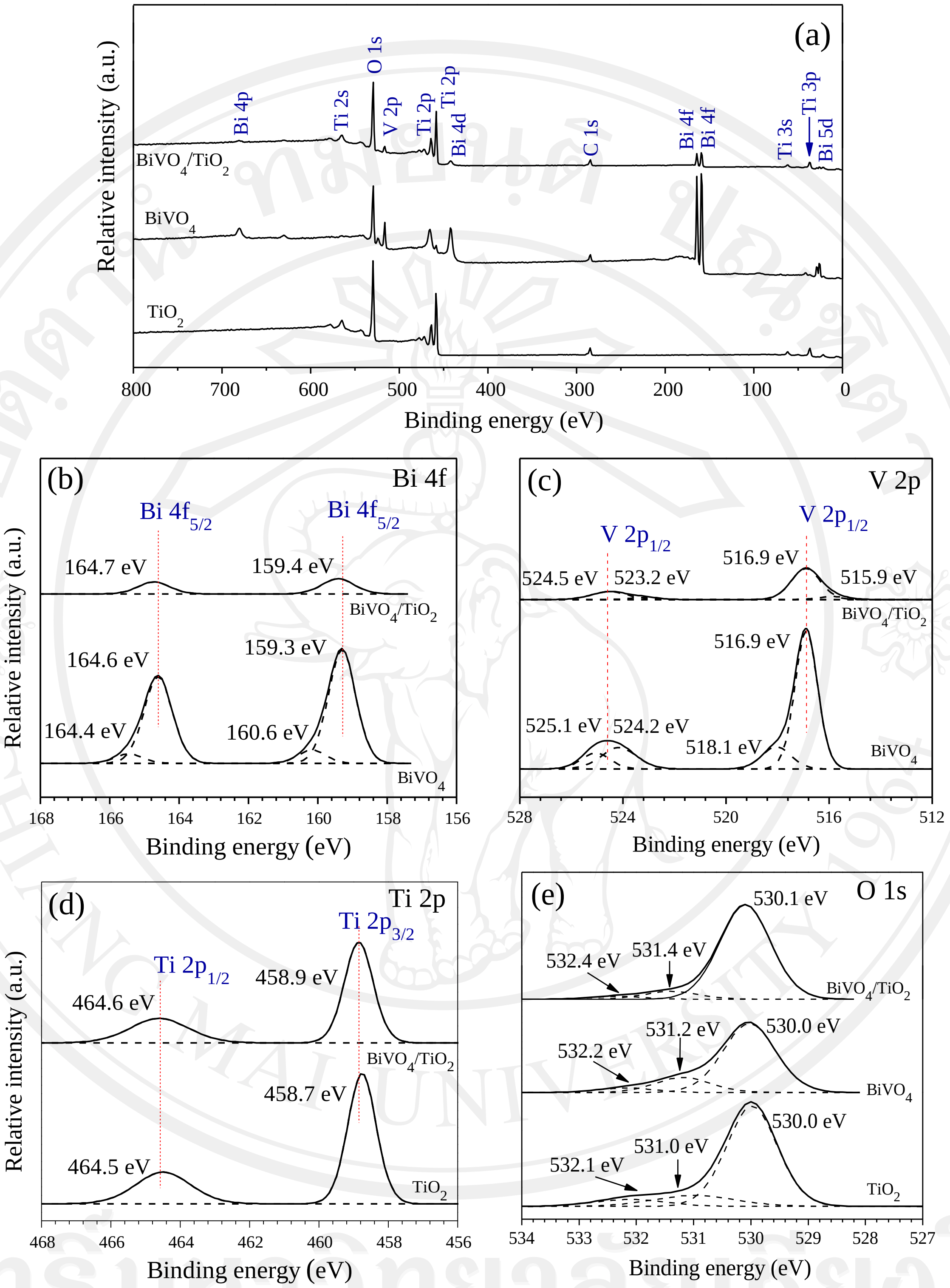

Figure 4.5 XPS survey spectra of the TiO_2, $BiVO_4$ and 1:1$BiVO_4/TiO_2$ composites, high-resolution XPS spectrum of (b) Bi 4f, (c) V 2p, (d) Ti 3d and (e) O 1s regions.

the C 1s transition at 284.6 eV was used as a reference to calibrate the binding energies of other elements. The high resolution XPS spectra of 1:1$BiVO_4$/TiO_2 composite showed the binding energy spectra splitting of Bi $4f_{7/2}$ and Bi $4f_{5/2}$ at 159.4 and 164.7 eV, respectively (Figure 4.5(b)), which was assigned to Bi^{3+} of $BiVO_4$ presented in separate phase [10]. The two symmetric spectra of V $2p_{1/2}$ and V $2p_{3/2}$ in the 1:1$BiVO_4$/TiO_2 composite at binding energies of 524.4 and 516.9 eV, respectively (shown in Figure 4.5(c)), were characteristic of V^{5+} ions [10]. In Figure 4.5(d), the 1:1$BiVO_4$/TiO_2 composite presented two spectra of Ti 2p at 458.9 and 464.6 eV assigned to Ti $2p_{3/2}$ and Ti $2p_{1/2}$, respectively. The spectrum separation between Ti 2p3/2 and Ti 2p1/2 was 5.7 eV, which was the expected oxidation state of Ti^{4+} [27, 32]. No indicated peaks as reduced Ti^{3+} was observed in the spectra. The O 1s spectrum was located at 530.1 eV with an asymmetric pattern as in showed Figure 4.5(d). The primary spectrum at 530.1 eV indicated the O^{2-} ion, while the additional shoulders at higher energies assigned to surface OH^- groups and/or chemisorbed H_2O [33].

Moreover, to further investigate the formation of TiO_2 on $BiVO_4$ of the 1:1$BiVO_4$/TiO_2 composite, which were performed with transmission electron microscopy (TEM) and TEM images are shown in Figure 4.6. Figure 4.6 (a) shows TEM image of 1:1$BiVO_4$/TiO_2 composite, it was found that small nanoparticles of TiO_2 with the average size of 10–30 nm are completely covered onto the surface of the $BiVO_4$ with a size of 80 nm. The diffraction rings of corresponding selected area electron diffraction (SAED) pattern of 1:1$BiVO_4$/TiO_2 composite in Figure 4.6 (b) can be indexed as (112) and (200) lattice planes of $BiVO_4$, which came along with (101), (004), (200), (105) and (204) lattice planes of TiO_2. To confirm the morphologies of TiO_2 and $BiVO_4$ in the 1:1$BiVO_4$/TiO_2 composite, TEM images of pure TiO_2 and $BiVO_4$ nanoparticles and their corresponding SAED pattern were also investigated. It could be observed that the TEM image of pure TiO_2 (Figure 4.6 (c)) revealed a small nanoparticle with similar to the small particles in Figure 4.6 (a). In the case of pure $BiVO_4$, it showed a large aggregated particle related to the $BiVO_4$ particles in the composites as shown in Figure 4.6 (a). However, this large particle also consisted of lots of nanoparticles with a size about 5–40 nm as shown in Figure 4.6 (e). The SAED patterns of the pure TiO_2 (Figure 4.6 (d)) and $BiVO_4$ (Figure 4.6 (f)) indicated that they were polycrystalline and could be indexed to tetragonal TiO_2 (JCPDS 21–1271) and monoclinic $BiVO_4$ (JCPDS 75–1866), respectively, which agreed well with the XRD results in Figure 4.3.

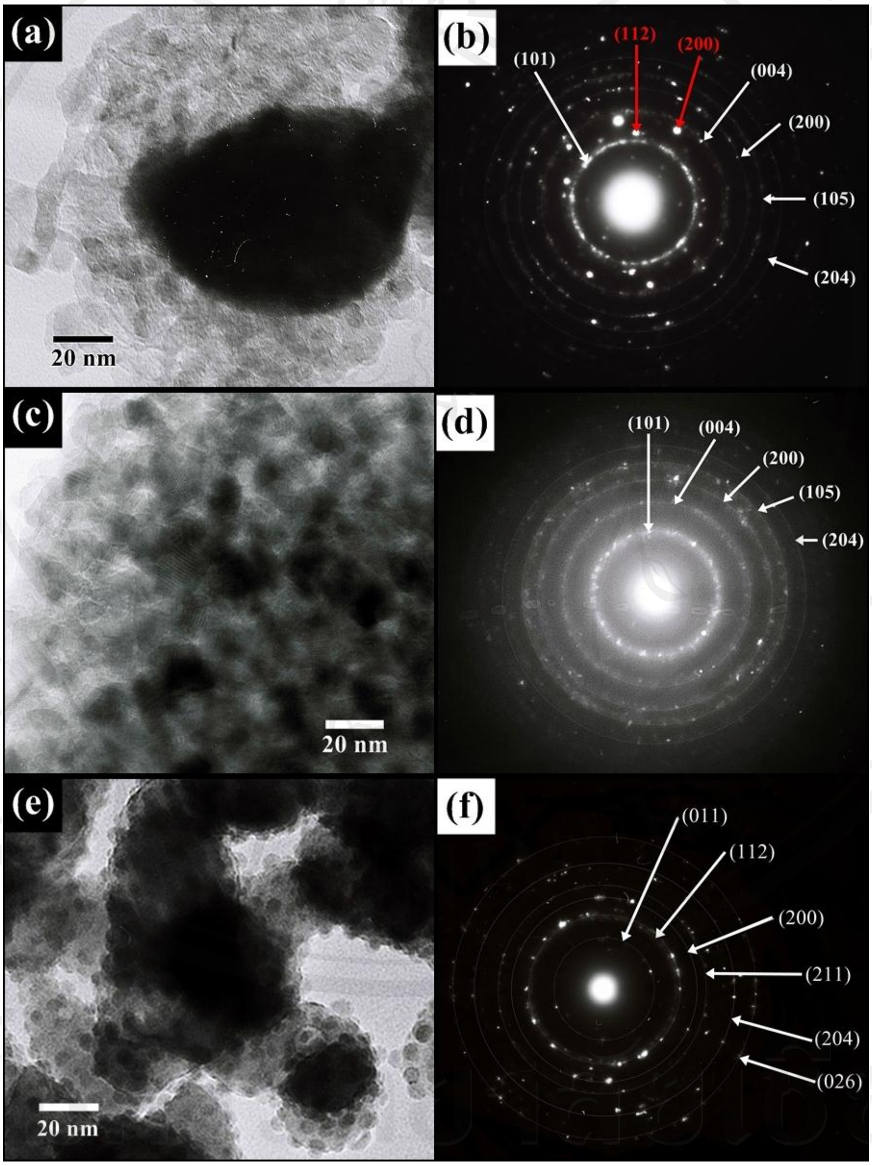

Figure 4.6 TEM images and corresponding SAEDs (a) and (b) of 1:1$BiVO_4$/TiO_2 composite, (c) and (d) of TiO_2 nanoparticles, and (e) and (f) of $BiVO_4$ particles, respectively.

4.3.2 Characterization of $BiVO_4/TiO_2$ composite films

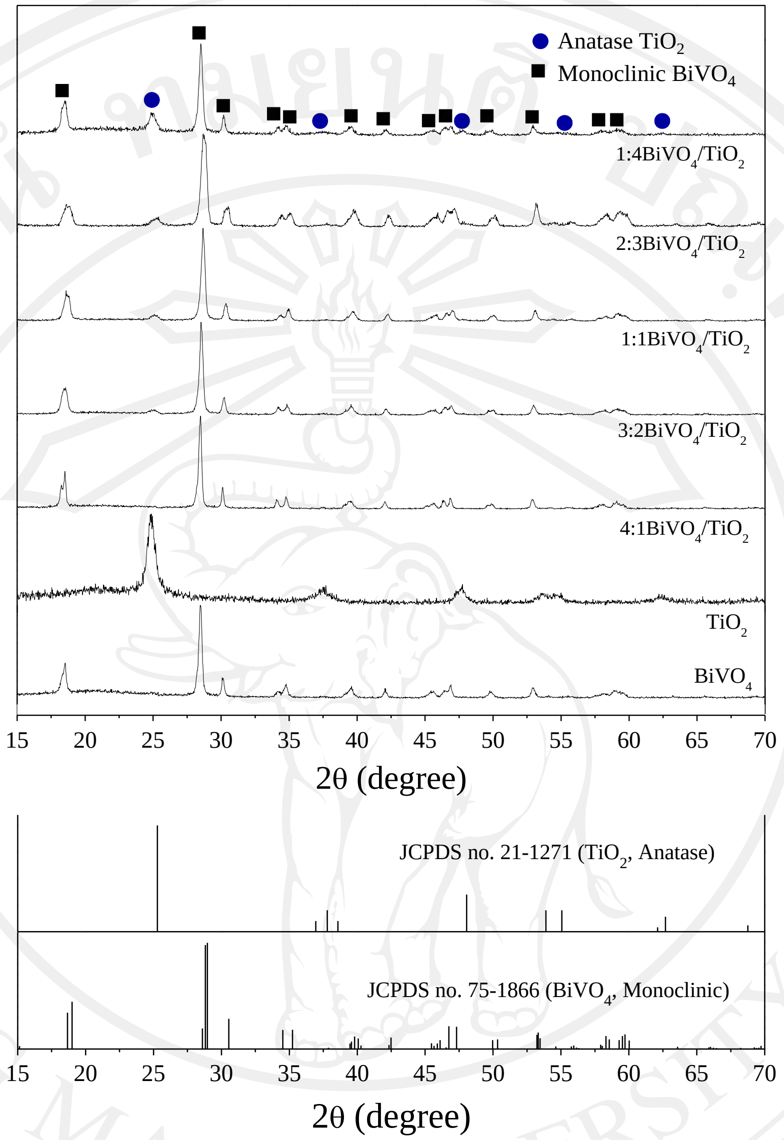

Figure 4.7 XRD patterns of pure $BiVO_4$, pure TiO_2 and $BiVO_4/TiO_2$ composite films with different mole ratios annealed at 500ºC for 1 h.

In order to solve the catalysts separation issue for studying their photocatalytic activities, the photocatalysts ($BiVO_4$, TiO_2 and $BiVO_4/TiO_2$ composites with different mole ratios) in film forms were fabricated by a doctor blading technique on glass substrates. Figure 4.7 shows the XRD patterns of the $BiVO_4$ films fabricated on glass substrate by doctor blading method using the above photocatalysts and annealed at 500ºC for 1 h. XRD patterns exhibited characteristic diffraction peaks of both monoclinic

$BiVO_4$ (JCPDS 75–1688) and tetragonal TiO_2 (JCPDS 21–1271) crystalline phases similarly with the XRD results of the composite powders and no evidence of any third phase. Moreover, the XRD patterns of all prepared films (TiO_2, $BiVO_4$, and $BiVO_4/TiO_2$ composites) obtained sharper than the XRD patterns of their powders (Figure 4.3) indicating higher crystalline sizes as shown in Table 4.3.

Table 4.3 Comparison of phase composition and crystalline size of $BiVO_4/TiO_2$ composite films with different mole ratios after annealing at 500ºC for 1 h.

Samples	**Phase composition (%)**		**Crystalline size (nm)**	
	$BiVO_4$	**TiO_2**	**$BiVO_4$**	**TiO_2**
$BiVO_4$	100	-	18.09	-
4:1$BiVO_4/TiO_2$	100	-	18.84	-
3:2$BiVO_4/TiO_2$	95.56	4.44	10.48	7.59
1:1$BiVO_4/TiO_2$	93.73	6.27	15.09	7.02
2:3$BiVO_4/TiO_2$	90.88	9.12	15.73	6.10
1:4$BiVO_4/TiO_2$	81.27	18.73	23.55	8.26
TiO_2	-	100	-	6.68

Light adsorption properties of the $BiVO_4/TiO_2$ composites with different mole ratios were also investigated by UV-vis diffuse reflectance spectroscopy, which are presented in Figure 4.8 (a) transmission, (b) refraction and (c) absorption spectra in the range of 300–700 nm. Comparing to the pure $BiVO_4$, the absorption edges of all $BiVO_4/TiO_2$ composite films showed lower wavelengths of about 440–460 nm. There was no such tendency for the $BiVO_4/TiO_2$ composite films when increasing the mole ratio of $BiVO_4$. The experimentally determined band gaps were calculated according to the Equation (2.1). The band gaps of the as-prepared composite films estimated from the intercept of the plots of $(\alpha h\nu)^2$ versus $h\nu$ illustrated in Figure 4.8 (d) and Table 4.3. It was found that the 1:1$BiVO_4/TiO_2$ composite showed high adsorption in visible region (520–700 nm) and its band gap (2.43 eV) was closeness to the pure $BiVO_4$ (2.45

eV). These results indicated that the optimum mole ratio of the $BiVO_4/TiO_2$ composite was for good visible light adsorption was 1:1, which agreed well with the photocatalytic test results.

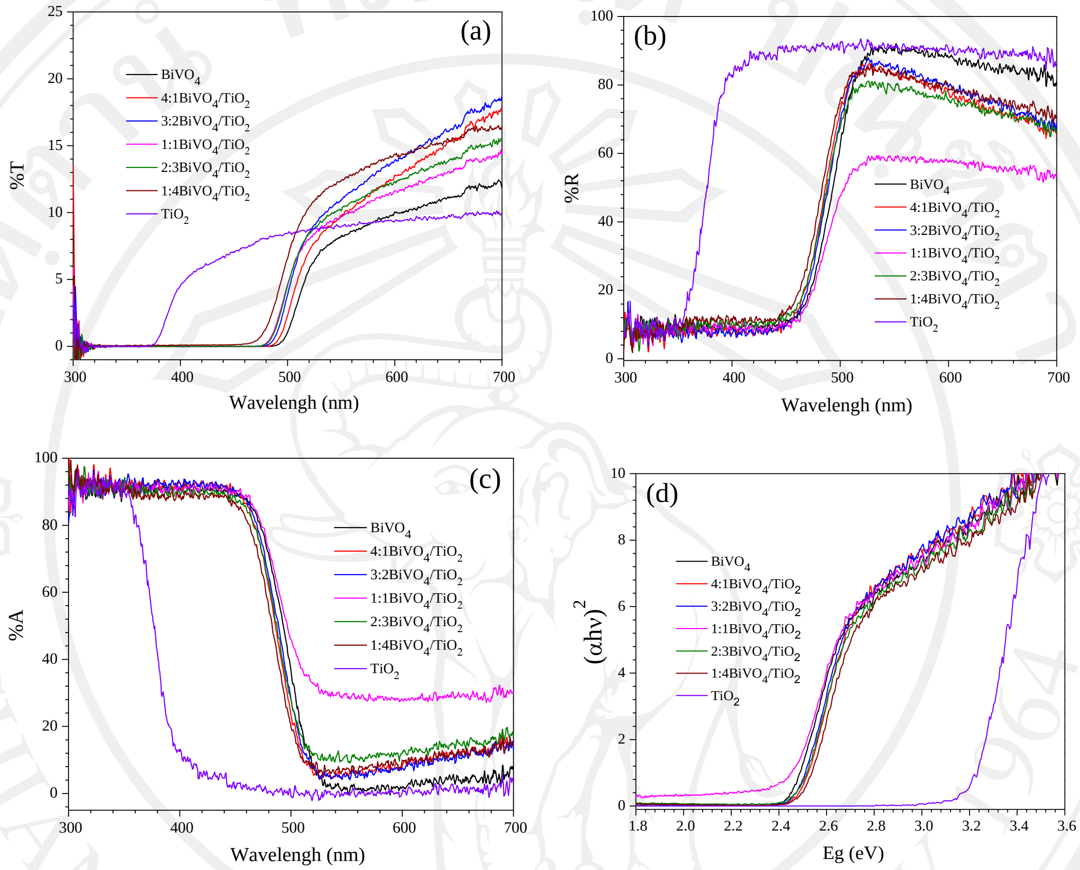

Figure 4.8 UV-vis diffuse (a) the transmission, (b) refraction and (c) absorption in the range of 300–700 nm absorption spectra and (d) the plots of $(\alpha h\nu)^2$ versus photon energy ($h\nu$) of pure $BiVO_4$, pure TiO_2 and $BiVO_4/TiO_2$ composite films with different mole ratio after annealing at 500ºC for 1 h.

4.2.3 Photocatalytic activities of $BiVO_4/TiO_2$ composite films

The photocatalytic activities of the $BiVO_4/TiO_2$ composite films were evaluated by a degradation of MB aqueous solution (50 μM) under visible light irradiation (<400 nm) as a test reaction according to the literature [11, 13, 22, 24]. The degradation of MB was monitored by examining in decreases of its concentration, which measured the changes in maximal absorption of UV-vis spectra at 664.5 nm. As shown in Figure 4.9, the maximum absorption peak of MB decreased gradually under visible light irradiation for 120 min in the presence of the $BiVO_4/TiO_2$ composite film. Figure 4.10 shows the adsorptive and photocatalytic efficiencies of the $BiVO_4/TiO_2$ composite films with different mole ratios for MB degradation was defined as C_t/C_0, where C_0 and C_t are the initial concentration and the concentration of MB during the reaction time, respectively. Moreover, the experiments of MB direct photolysis (without catalyst), pure TiO_2 and pure $BiVO_4$ films were also conducted to compare with the $BiVO_4/TiO_2$ composite films. It was found that the adsorptive efficiencies of all $BiVO_4/TiO_2$ composite films with different mole ratios were quite similar together corresponding to total surface are of the films calculated from the Brunauer Emmett Teller (BET) specific surface areas results as shown in Table 4.4.

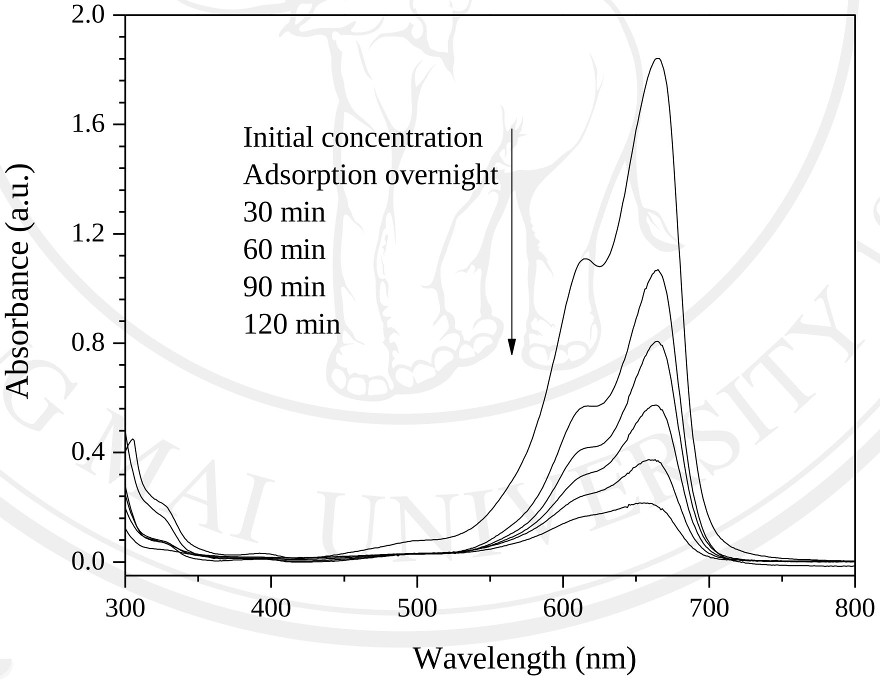

Figure 4.9 UV-vis spectra of MB with 1:1$BiVO_4/TiO_2$ composite film.

For the photocatalytic degradation of MB in the presence of $BiVO_4/TiO_2$ composite films demonstrated higher than the values obtained for pure TiO_2 (40%) and $BiVO_4$ (68%) films after irradiating for 120 min, which were 76%, 82%, 88%, 80% and 71% in the presence of

$1{:}4BiVO_4/TiO_2$, $2{:}3\ BiVO_4/TiO_2$, $1{:}1BiVO_4/TiO_2$, $3{:}2\ BiVO_4/TiO_2$ and $4{:}1BiVO_4/TiO_2$ composite films, respectively.

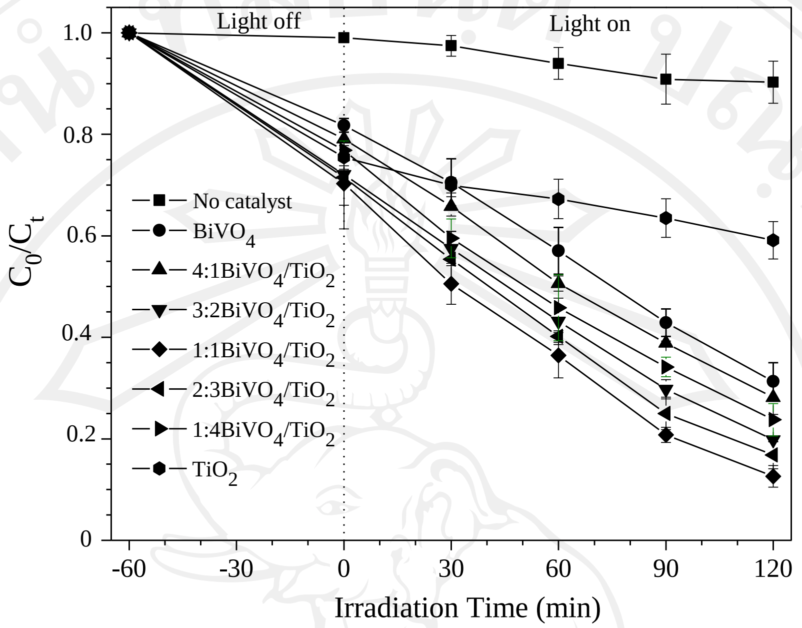

Figure 4.10 Photocatalytic efficiencies of $BiVO_4/TiO_2$ films with different ratios.

Table 4.4 The relationship between band gap energies (E_g), BET surface areas (S_{BET}), total area and degradation rate constant (k_{app}) of MB solution over $BiVO_4/TiO_2$ composite films with different mole ratios.

Sample films	**Properties**			
	E_g (eV)	**S_{BET} (m^2g^{-1})**	**total area (cm^2)**	**k_{app} (h^{-1})**
$BiVO_4$	2.45	15.40	1540	0.564 ± 0.043
$4{:}1BiVO_4/TiO_2$	2.48	5.77	577	1.046 ± 0.095
$3{:}2BiVO_4/TiO_2$	2.47	13.57	1357	1.375± 0.116
$1{:}1BiVO_4/TiO_2$	2.43	27.88	2788	1.569 ± 0.049
$2{:}3BiVO_4/TiO_2$	2.48	32.01	3201	1.358 ± 0.119
$1{:}4BiVO_4/TiO_2$	2.49	49.86	4986	1.253 ± 0.085
TiO_2	3.20	71.05	7105	0.362 ± 0.150

In order to quantitatively understand photocatalytic degradation of MB, the pseudo-first order kinetic model as displayed by Equation (1.35) in Chapter 1 was applied for all of synthesized composite films. The pseudo-first order rate constants for the pure TiO_2, pure $BiVO_4$, 1:4$BiVO_4/TiO_2$, 2:3$BiVO_4/TiO_2$, 1:1$BiVO_4/TiO_2$, 3:2$BiVO_4/TiO_2$ and 4:1$BiVO_4/TiO_2$ composite films were 0.362 ± 0.150, 0.564 ± 0.043, 1.253 ± 0.085, 1.358 ± 0.119, 1.569 ± 0.049, 1.375± 0.116, and 1.046 ± 0.095 h^{-1}, respectively, as shown in Figure 4.11. From the comparison of the pseudo-first order rate constants, it could be concluded that optimum condition for synthesis the composite photocatalyst of $BiVO_4/TiO_2$ for degradation of MB was 1:1.

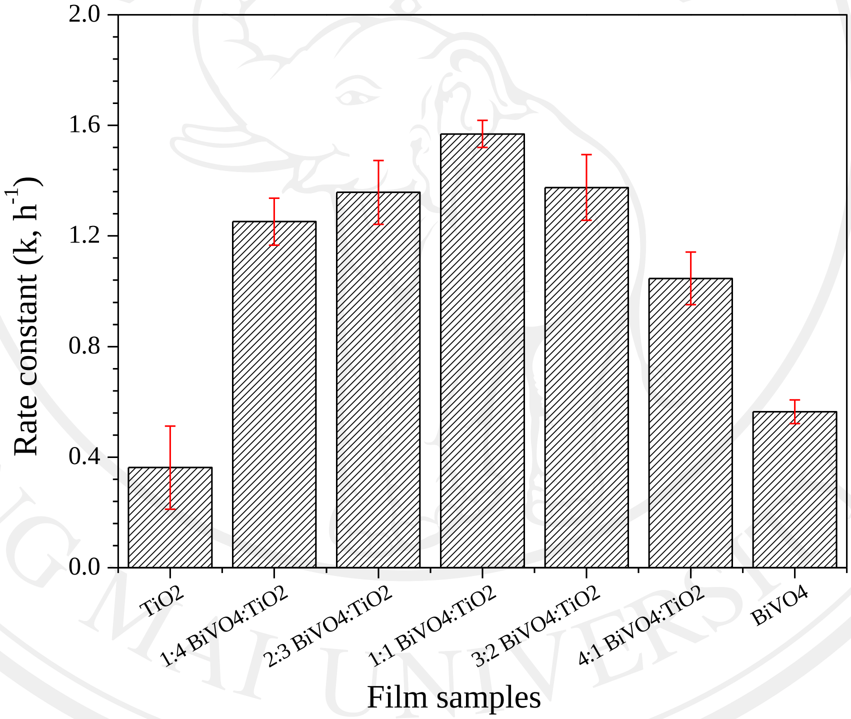

Figure 4.11 First order rate constants of photodegradation of MB by using $BiVO_4$, $BiVO_4$, TiO_2 and $BiVO_4/TiO_2$ composite films with different mole ratio under irradiation of visible light.

Based on the enhanced photocatalytic activity of the $BiVO_4/TiO_2$ composite photocatalyst for degradation of MB under visible light irradiation, a possible mechanism of photogenerated charge separation at the interface of heterojunction $BiVO_4/TiO_2$ composite and its photocatalytic process can be proposed as presented in Figure 4.12. The conduction band (CB) and valence band (VB) positions can be determined by using the following Equation (4.1) which is similar to the Equation (2.3) in Chapter 2 [34].

$$E_{CB} = \chi - E_e - 0.5E_g \qquad (4.1)$$

where E_{CB} denotes the CB edge potential, χ is the absolute electronegativity of the semiconductor (5.90 eV [35] and 6.04 eV [36] for TiO_2 and $BiVO_4$, respectively), E_e is the energy of free electrons on the hydrogen scale (about 4.5 eV) and E_g is the band gap of the semiconductor (3.20 and 2.45 eV for TiO_2 and $BiVO_4$, respectively). The position of the VB edge is determined by $E_{VB} = E_{CB} + E_g$. The calculated CB and VB of TiO_2 were −0.20 and 3.00 eV, and of $BiVO_4$ were 0.31 and 2.76 eV, respectively, which agreed well to the mechanism of $BiVO_4/TiO_2$ heterojunction reported clearly by Hu *et al.* [14] and Zhang *et al.* [15].

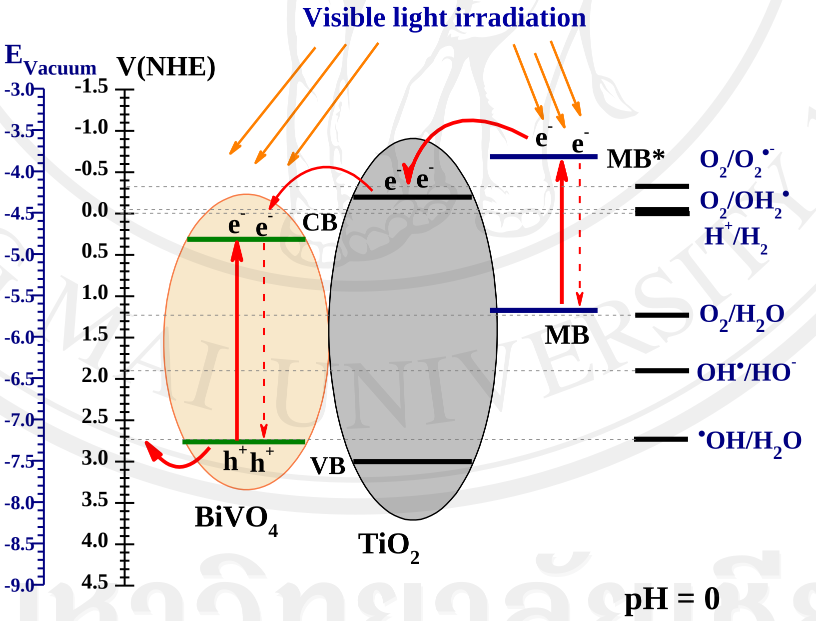

Figure 4.12 Schematic diagram of charge separation of $BiVO_4/TiO_2$ heterostructure photocatalysts under visible light irradiation at pH 0.

Under visible light irradiation, MB can adsorb the visible light and then generate the exited MB*. Thus, the higher rates of MB degradation were recorded due to the increase of electron transfer from the exited MB* to the CB of TiO_2 and then the electrons at CB of TiO_2 will then be transferred to the oxygen molecules adsorbed on the surface of TiO_2 [37]. Simultaneously, $BiVO_4$ can be activated by visible light and generated electron and hole pairs. However, there are excess electrons at the CB of $BiVO_4$ with transferred from the CB of TiO_2, lead to increase recombination rate between electrons and holes in $BiVO_4$. Therefore, the main reaction to produce strong oxidizing radicals is the reduction of surface chemisorbed O_2 to $O_2^{\bullet-}$ by the electron at the CB of TiO_2, which these strong oxidizing radicals can degrade the MB molecules to finally H_2O, CO_2, NO_3^-, and SO_4^{2-} [38].

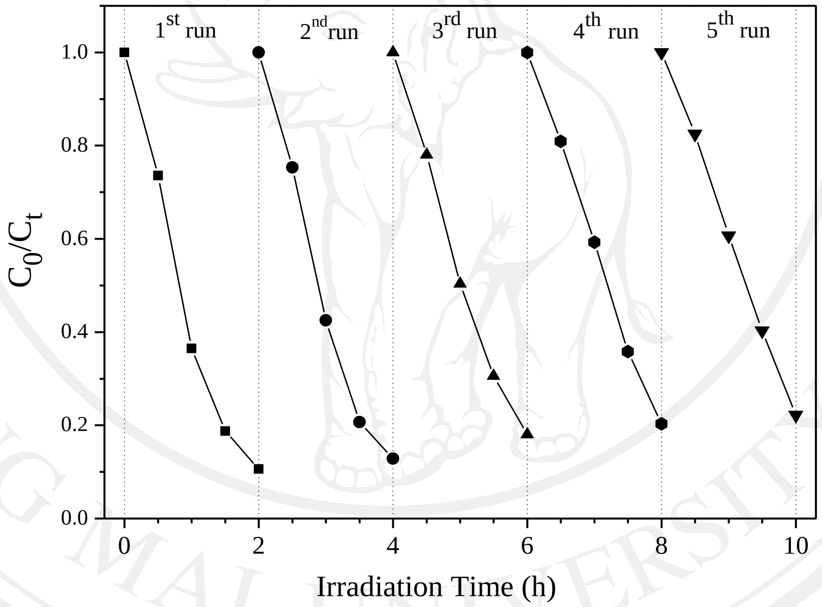

Figure 4.13 Recycling runs of methylene blue solution in the photodegradation on 1:1$BiVO_4/TiO_2$ photocatalytic film.

In order to evaluate the photostability of the 1:1$BiVO_4/TiO_2$ composite film, the experiments were carried out for five runs in the same experimental conditions. After each photocatalytic reaction, the 1:1$BiVO_4/TiO_2$ composite film was annealed at 250ºC for 1 h to remove the adsorbed organic contaminants on the photcatalyst surface. The result (Figure 4.13) clearly revealed that the photocatalytic efficiency did not show significant loss after five recycles, indicating that the 1:1$BiVO_4$/TiO_2 composite film was high stability and not photocorroded during the whole degradation processes.

4.4 Results and discussion for $BiVO_4$/WO_3 composites

4.4.1 Characterization of $BiVO_4$/WO_3 composite powders

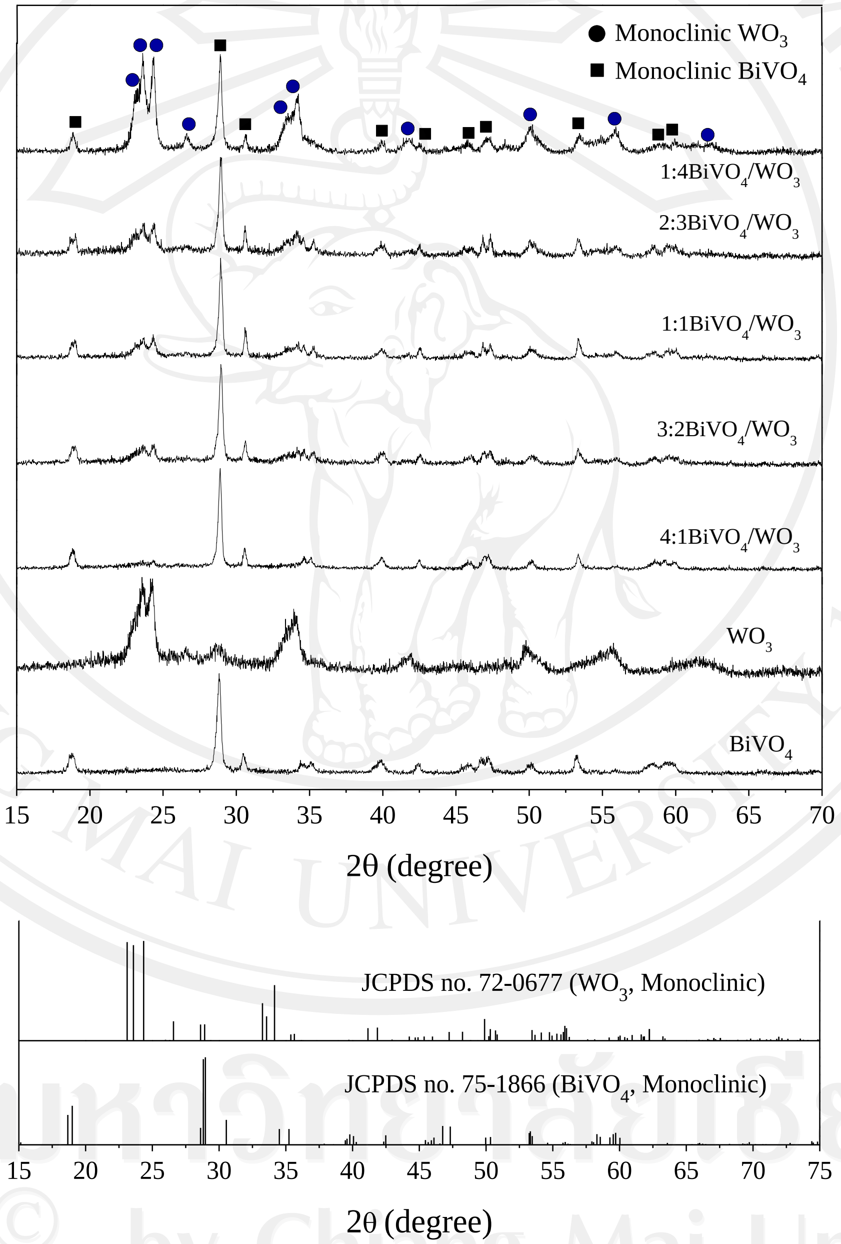

Figure 4.14 XRD patterns of pure $BiVO_4$ powder, pure WO_3 powder and $BiVO_4$/WO_3 composite powder with different mole ratios after calcination.

Table 4.5 Comparison of phase compositions and crystalline sizes of $BiVO_4/WO_3$ composite powders with different mole ratios.

Sample	Phase composition (%)		Crystalline size (nm)	
	$BiVO_4$	WO_3	$BiVO_4$	WO_3
$BiVO_4$	100	-	18.84	-
4:1$BiVO_4/WO_3$	94.38	5.62	42.24	21.40
3:2$BiVO_4/WO_3$	84.39	15.61	42.24	19.48
1:1$BiVO_4/WO_3$	80.76	19.24	40.25	17.88
2:3$BiVO_4/WO_3$	73.96	26.04	38.45	20.22
1:4$BiVO_4/WO_3$	48.94	51.06	40.25	17.77
WO_3	-	100	-	23.08

The crystalline structure of the synthesized $BiVO_4/WO_3$ composite powders with different mole ratios of 1:4, 2:3, 1:1, 3:2, and 4:1 were determined using XRD compared to pure WO_3 and $BiVO_4$ as shown in Figure 4.14. For the XRD pattern of pure $BiVO_4$ powder, all peaks could be confirmed to be the monoclinic phase of $BiVO_4$, which matched well with the JCPDS file no. 75−1866. The XRD pattern of pure WO_3 powder was demonstrated that the diffraction peaks at 23.57°, 24.24°, 26.57°, 28.71°, 34.08°, 41.95°, 49.71°, 55.63° and 61.58° could be indexed to (020), (200), (120), (112), (202), (222), (400), (402) and (340) of the monoclinic WO_3 phase, respectively, which positions and their relative intensities were in good agreement with the standard diffraction data (JCPDS: 72−0677). XRD patterns of $BiVO_4/WO_3$ composite powders, it was obviously seen that the XRD peaks belonging to monoclinic $BiVO_4$ displayed as a major phase in all composite catalysts, and the XRD peaks belonging to monoclinic WO_3 was increased when increasing mole ratio of WO_3 as corresponded with the calculated percentage of phase composition and crystalline size in Table 4.5. It was revealed that the percentage of phase composition of $BiVO_4$ in the $BiVO_4/WO_3$ composites with mole ratios of 4:1, 3:2, 1:1 and 2:3 had higher than of WO_3 indicating more high cystallinity in $BiVO_4$ than WO_3. For the crystalline size, the pure $BiVO_4$ showed smaller that the $BiVO_4$ of the composites, this probably due to the covered WO_3 particles on the surface of the $BiVO_4$ particles.

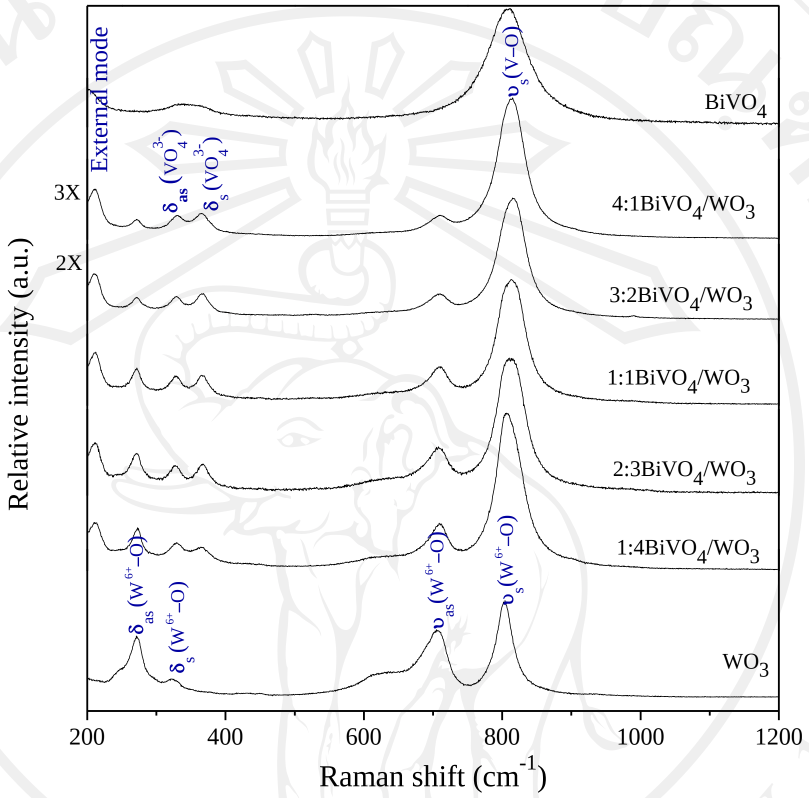

Figure 4.15 Raman spectra of pure $BiVO_4$, pure WO_3 and $BiVO_4/WO_3$ composite powder with different mole ratios.

Raman spectroscopy was used to further confirmation of the obtained both structures ($BiVO_4$ and WO_3) in the $BiVO_4/WO_3$ composite. As shown in Figure 4.15 shows Raman spectra the $BiVO_4/WO_3$ composites with different mole ratios of 4:1, 3:2, 1:1, 2:3 and 1:4 compared to pure $BiVO_4$ and WO_3. The pure WO_3 powder shows characteristic vibration modes of Raman spectra at 271.4, 324.0, 705.9 and 806.8 cm^{-1} [37]. The observed spectra at 271.4 and 324.0 cm^{-1} were attributed to the asymmetric and symmetric bending vibration of O–W–O, respectively, whereas, the spectra at 705.9 and 806.8 cm^{-1} were attributed to the asymmetric and symmetric O–W–O stretching vibrations respectively [37, 39]. All these spectra were the the characteristic features of monoclinic WO_3. For the pure $BiVO_4$ powder, all Raman spectra were vibrational bands of monoclinic $BiVO_4$ agreeing well with the reported works [28, 29]. Obviously in the $BiVO_4/WO_3$ composites, the spectrum belonging to $BiVO_4$ at 810.5 cm^{-1} overlapped with WO_3 at 806.8 cm^{-1}, which lead to the boarded spectrum in this position. Thus, the Raman analyse confirmed the presence of WO_3 in the $BiVO_4/WO_3$ composites agreeing with the XRD results, which indicated that WO_3 was present as a separated crystalline phase.

Furthermore, the surface composition and the chemical state of the 1:4$BiVO_4$/ WO_3 composite of was analysed by XPS to be compared with pure WO_3 and $BiVO_4$. Figure 4.16 (a) shows the comparison of survey XPS spectra of pure WO_3 and pure $BiVO_4$ and 4:1$BiVO_4/WO_3$ composite, which can observe the spectra corresponding to Bi, W, C, V and O. For the 4:1 $BiVO_4/WO_3$composite, the Bi 4f spectra with the binding energy peaks splitting at 159.7 and 167.1 eV were attributed to be o Bi $4f_{7/2}$ and Bi $4f_{5/2}$, respectively, which is assigned to Bi^{3+} of $BiVO_4$ present in separate phase (Figure 41.6(b)) [10]. The two symmetric spectra of V $2p_{1/2}$ and V $2p_{3/2}$ in the 4:1$BiVO_4/WO_3$ composite at binding energies of 525.0 and 517.4 eV respectively (shown in Figure 4.16(c)), are characteristic of V^{5+} ions [10]. The spectra of W at 35.9 and 38.0 eV which are shown in Figure 4.16(d) can be attributed to the W $4f_{7/2}$ and W $4f_{5/2}$ binding energies, respectively, which was suggested that W^{6+} was deposited in the form of WO_3 agreeing with the reported literature values [6] and [40]. When compared with the pure $BiVO_4$ and pure WO_3 the Bi 4f, V 2p and W 4f spectra of the 4:1$BiVO_4/WO_3$ composite slightly shifted to the high binding energies, indicating an interaction between the $BiVO_4$ and WO_3 on the surface of the composite. The O1s binding energies of the pure $BiVO_4$, pure WO_3, and 4:1$BiVO_4/WO_3$ composite are shown in Figure 4.16(e) located at 529.85, 529.85 and 530.05 eV, respectively. Compared to the pure $BiVO_4$ and pure WO_3, the O1s became broader and there was a slight increase in binding energy in the 1:1$BiVO_4/WO_3$ composite. This positive shift inferred the W–O–Bi linkage which contains contributions from both the Bi–O and W–O, respectively [40, 41].

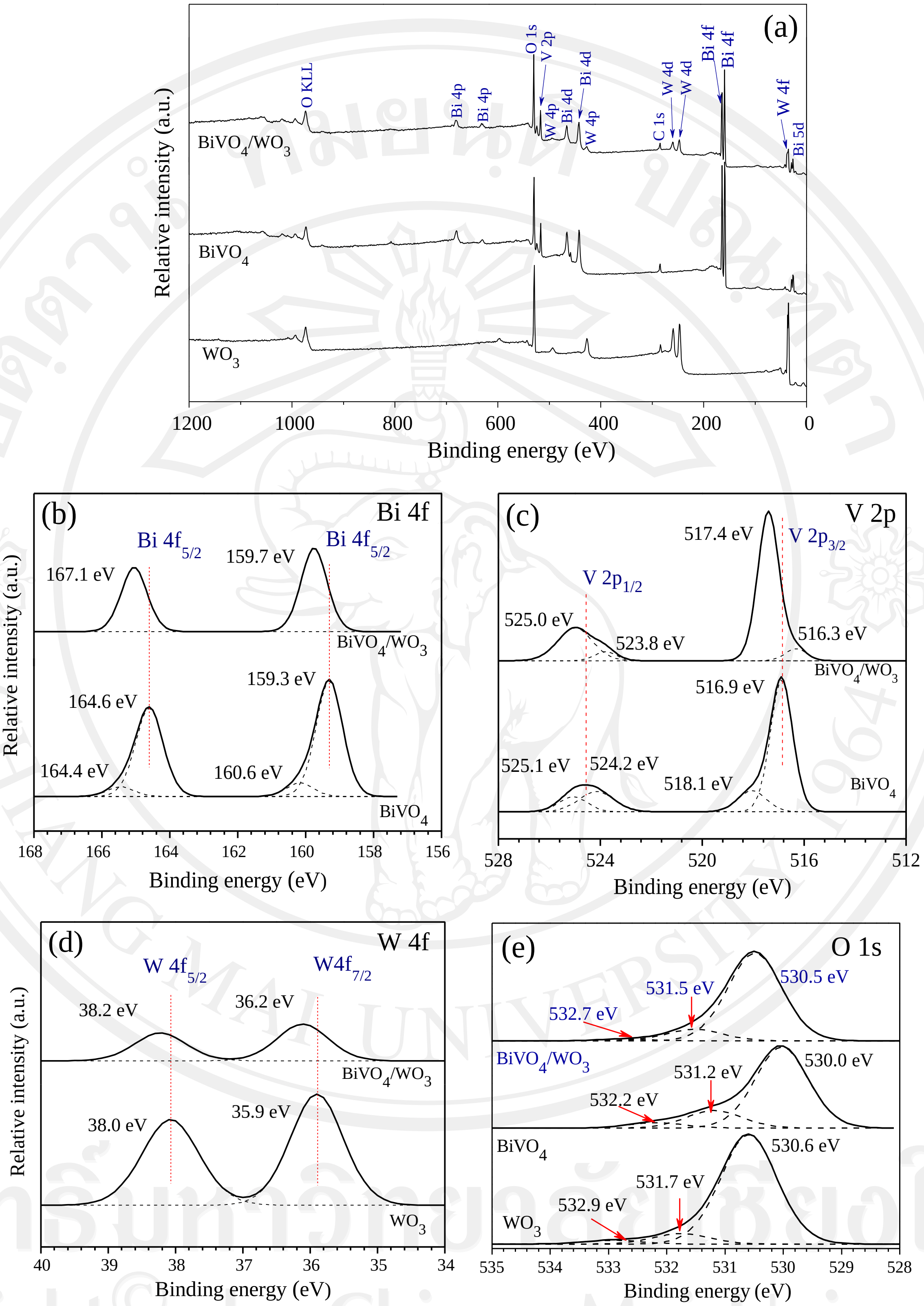

Figure 4.16 XPS survey spectra of the BiVO$_4$, WO$_3$ and 4:1BiVO$_4$/WO$_3$ composites, high-resolution XPS spectrum of (b) Bi 4f, (c) V 2p, (d) W 3d and (e) O 1s regions.

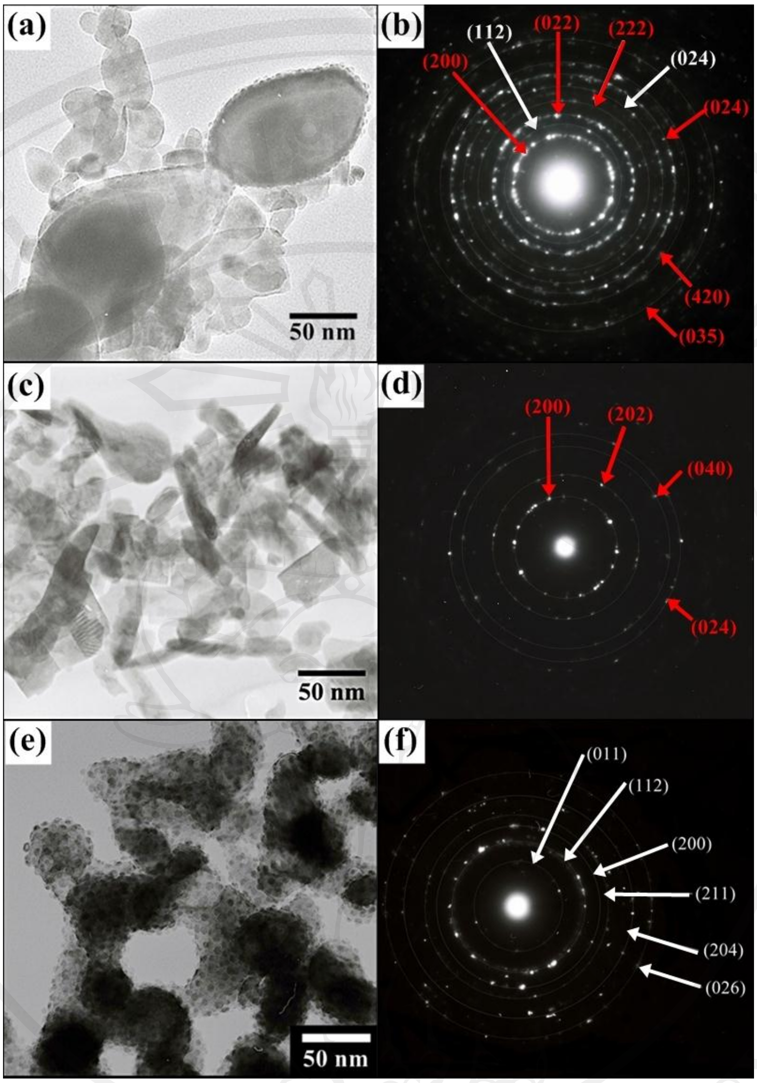

Figure 4.17 TEM images and corresponding SAEDs of (a) and (b) 4:1$BiVO_4/WO_3$ composite, (c) and (d) WO_3, and (e), (f) $BiVO_4$ nanoparticle, respectively.

The TEM characterization results on the 4:1$BiVO_4/WO_3$ composite and its corresponding SAED are shown in Figure 4.17(a) and Figure 4.17(b), respectively compared to the pure WO_3 (Figure 4.17(c) and Figure 4.17(d)) and pure $BiVO_4$ Figure 4.17(e) and Figure 4.17(f). The 1:1$BiVO_4/WO_3$composite in Figure 4.17(a) revealed large particles of $BiVO_4$ with diameter in the range of 60–100 nm, which related to the particles of pure $BiVO_4$ in Figure 4.17(e). Additionally, there were some smaller uninform particles (spherical-, rod- and plate-like) with particle size in the range of 10–60 nm contacted on the surface of $BiVO_4$ in the composite sample, corresponded to the obtained particles of pure WO_3 in Figure 4.17(c). In Figure 4.17(b), the corresponding SAED of 1:1$BiVO_4/WO_3$ composite was composed of two sets of diffraction patterns including monoclinic $BiVO_4$ (JCPDS: 75−1866) and monoclinic WO_3 (JCPDS: 72−0677), which agreed well with the XRD results. Thus, it was confirmed that the formation of this material was a composite of two metal oxides rather than doping materials.

4.4.2 Characterization of $BiVO_4/WO_3$ composite films

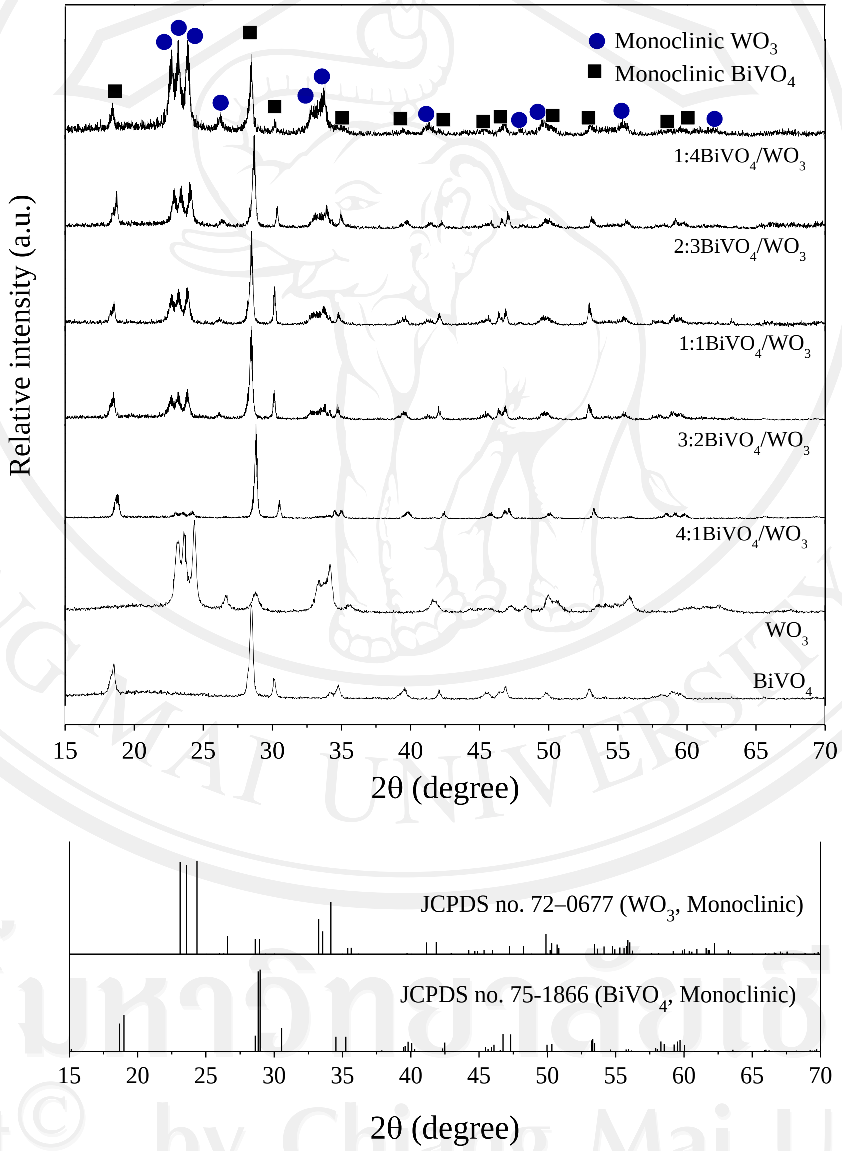

Figure 4.18 XRD patterns of pure $BiVO_4$, pure WO_3 and $BiVO_4/WO_3$ composite films with different mole ratios annealed at 500ºC for 1 h.

Table 4.6 Comparison of phase compositions and crystalline sizes of $BiVO_4/WO_3$ composite films with different mole ratios.

Sample	**Phase composition (%)**		**Crystalline size (nm)**	
	$BiVO_4$	**WO_3**	**$BiVO_4$**	**WO_3**
$BiVO_4$	100	-	18.09	-
$4{:}1BiVO_4/WO_3$	93.29	6.71	24.63	13.35
$3{:}2BiVO_4/WO_3$	76.16	23.84	29.06	15.53
$1{:}1BiVO_4/WO_3$	71.54	28.46	31.40	17.51
$2{:}3BiVO_4/WO_3$	67.17	32.83	28.30	16.49
$1{:}4BiVO_4/WO_3$	46.87	53.13	31.20	14.01
WO_3	-	100	-	16.49

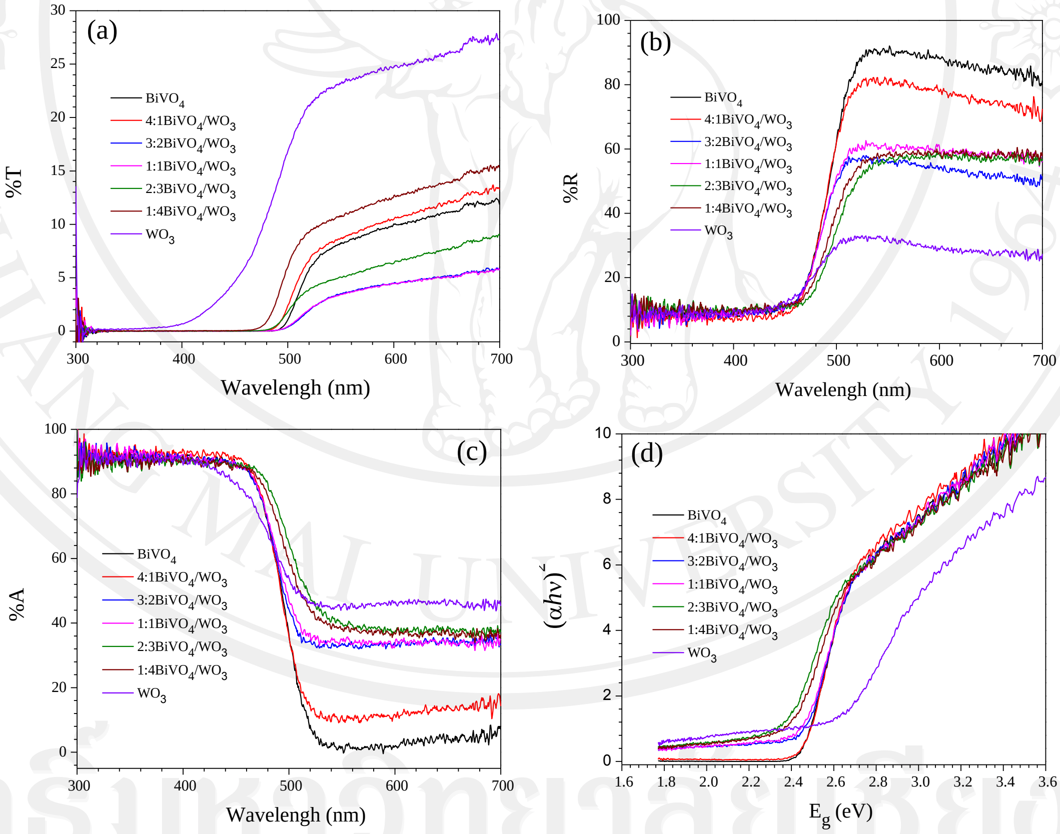

Figure 4.19 UV-vis diffuse absorption spectra of pure $BiVO_4$, pure WO_3 and $BiVO_4/WO_3$ composite films with different mole ratio after annealing at 500ºC for 1 h of (a) the transmission, (b) refraction and (c) absorption in the range of 500–800 nm and (d) the plots of $(\alpha h\nu)^2$ versus photon energy ($h\nu$).

Figure 4.19 shows (a) transmission, (b) refraction and (c) absorption spectra in the range of 300–700 nm of the pure WO_3, pure $BiVO_4$ and $BiVO_4/WO_3$ composites containing of 1:4, 2:3, 1:1, 3:2 and 4:1 mole ratios, which were investigated by UV-vis spectrophotometer. It was found that the absorption edges of all $BiVO_4/WO_3$ composite films were similar to pure $BiVO_4$ with in the range of 500–560 nm. Moreover, the band gap energies of all samples were evaluated using the Equation (2.1) as previously reported in Chapter 2, in which the intercept of the plots of $(\alpha h\nu)^2$ versus $h\nu$ were estimated as band gap energies of the photocatalysts films as illustrated in Figure 4.19(d) and Table 4.7. It is showed that the band gap energies of $BiVO_4/WO_3$ composite films were decreased with increasing the mole ratios of $BiVO_4$ loading.

4.4.3 Photocatalytic activities of $BiVO_4/WO_3$ composite films

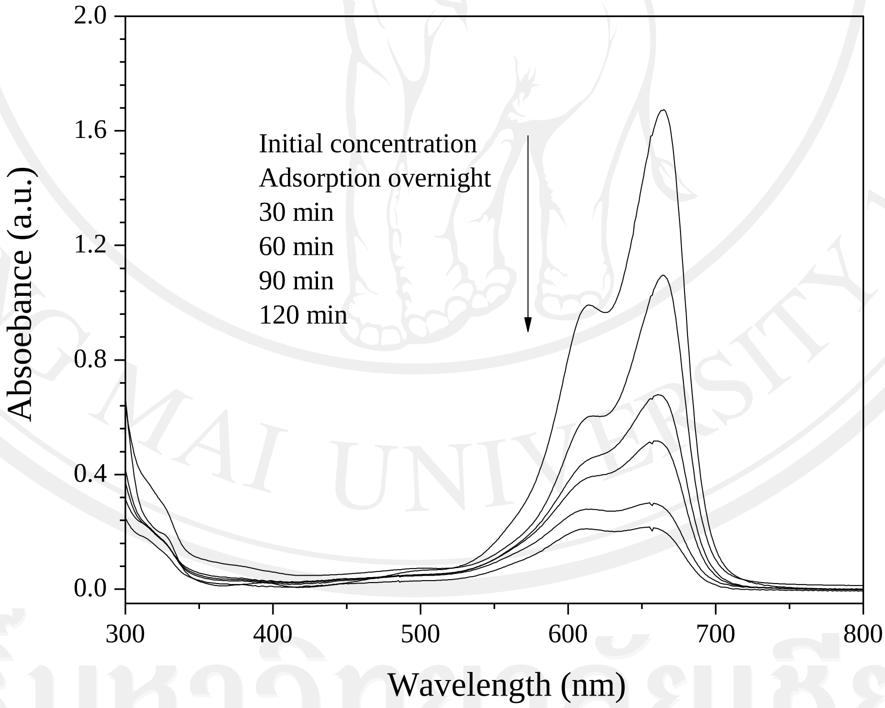

Figure 4.20 UV-vis spectra of MB with 4:1$BiVO_4/WO_3$ composite film.

The photocatalytic activities of the $BiVO_4/WO_3$ composite films with different mole ratios were also evaluated by a degradation of MB aqueous solution (50 μM) with the catalyst loading of ~0.1 g/L under visible light irradiation and compared to the pure WO_3 and $BiVO_4$ films. The time dependent absorption spectrum for the photocatalytic degradation of MB by 4:1$BiVO_4/WO_3$ composite film under visible light irradiation is presented in Figure 4.20, which is clearly seen that the absorption of MB decrease when increasing irradiation time. Figure 4.21 shows the adsorptive and photocatalytic efficiencies of the pure WO_3 and pure $BiVO_4$ and $BiVO_4/WO_3$ composite films with different mole ratios for MB degradation. It was found that the adsorptive efficiency of the pure WO_3 was the highest due to showing more negatively charged surface (IEP =1.67) than the pure $BiVO_4$ (IEP =3.74) which was favored by cationic dye such as MB, and the adsorptive efficiencies of the $BiVO_4/WO_3$ composite films were also increased with increasing mole ratio of WO_3 and corresponding to their total surface area as shown in Table 4.7. In contrast, the photocatalytic efficiency of $BiVO_4/WO_3$ composite films was increased when increasing the mole ratio of $BiVO_4$, the 4:1 $BiVO_4/WO_3$ composite films exhibited the highest photocatalytic efficiency. Since, visible light can be harvested by the $BiVO_4$, corresponding to the estimated band gap of 2.45 eV as shown in Figure 4.19(d), which thus leads to higher harvest efficiency of sunlight, compared to the WO_3. Moreover, the pseudo-first order kinetic model as shown in Equation (1.35) in Chapter 1 was applied for all of synthesized composite films. The comparison of pseudo-first order rate constants for the pure WO_3, pure $BiVO_4$, 1:4, 3:2, 1:1, 2:3 and 4:1 mole ratio of the $BiVO_4/WO_3$ composite films were summarized as the bar graphs in Figure 4.22 and Table 4.7, which 4:1$BiVO_4/WO_3$ composite also showed the highest rate constant of 0.693±0.064 for degradation of MB under visible light irradiation

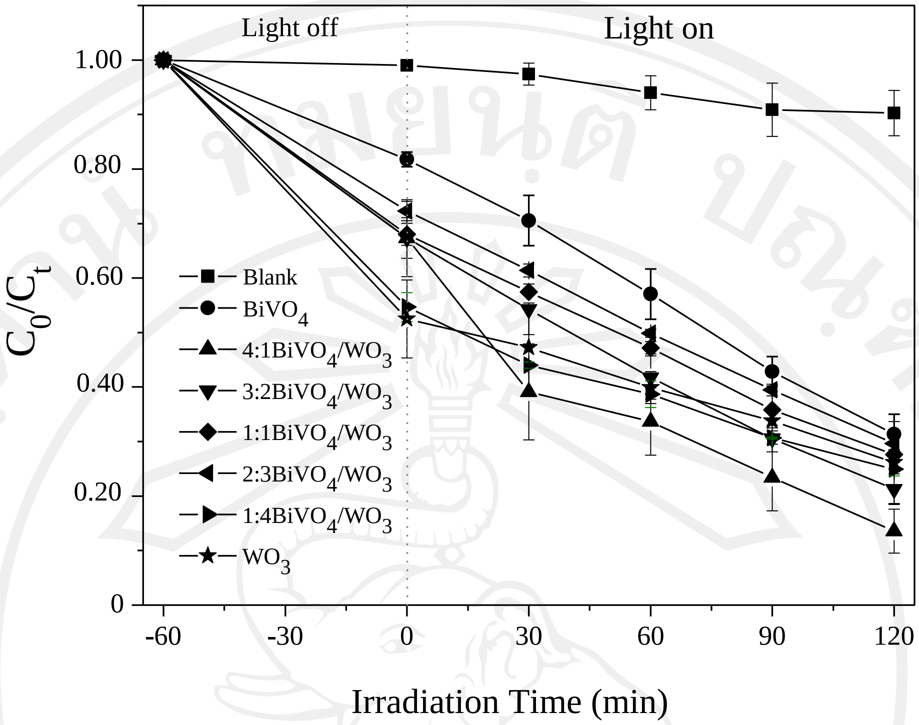

Figure 4.21 Photocatalytic efficiencies of composite films with different mole ratios.

Table 4.7 The relationship between BET surface areas (S_{BET}), band gap energies (E_g) and degradation rate constant (k_{app}) of methylene blue solution over $BiVO_4/WO_3$ composite films with different mole ratios.

Sample films	**Properties**			
	E_g (eV)	**S_{BET} (m^2g^{-1})**	**total area (cm^2)**	**k_{app} (h^{-1})**
$BiVO_4$	2.45	15.40	1540	0.564 ± 0.021
$4:1BiVO_4/ WO_3$	2.39	8.61	861	0.693 ± 0.064
$3:2BiVO_4/ WO_3$	2.41	10.00	1000	0.628 ± 0.119
$1:1BiVO_4/ WO_3$	2.43	14.61	1461	0.558 ± 0.065
$2:3BiVO_4/ WO_3$	2.44	15.98	1598	0.521 ± 0.130
$1:4BiVO_4/ WO_3$	2.47	18.06	1806	0.380 ± 0.147
WO_3	2.58	26.36	2636	0.315 ± 0.114

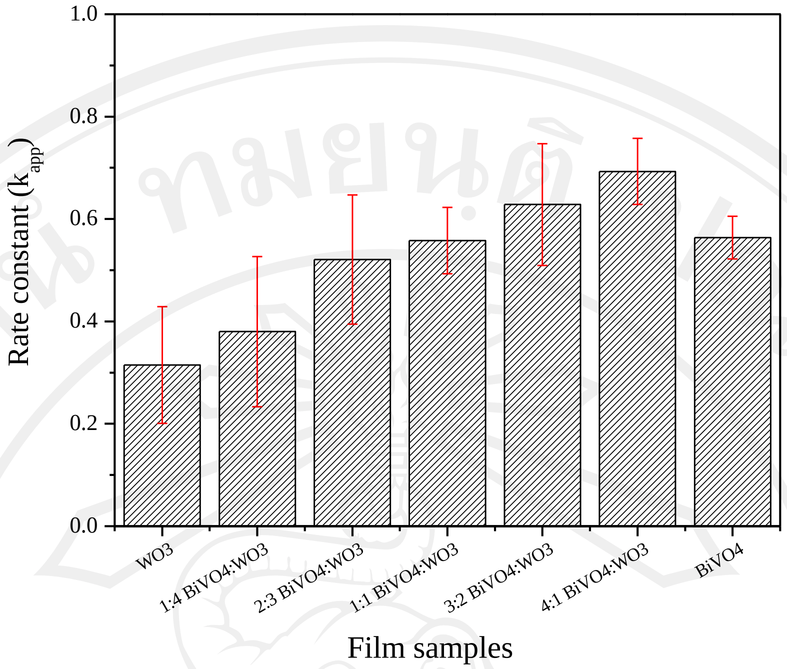

Figure 4.22 First order rate constants of photodegradation of MB by using $BiVO_4$, WO_3 and $BiVO_4/WO_3$ composite films with different mole ratios under visible light irradiation.

In order to understand more about the mechanism of the $4{:}1BiVO_4/WO_3$ photocatalyst for degradation of MB, the proposed diagram for their energy band edges and separation of electron-hole pairs are illustrated in Figure 4.23. It was believed that the enhancement of photocatalytic activity of the $4{:}1BiVO_4/WO_3$ composite was attributed to charge transfer at the heterojunction interfaces between $BiVO_4$ and WO_3 with matching band potentials, which consequently favoured an effective photoexcited electron hole separation in the two materials. Thus, the estimated CB and VB positions were 0.31 and 2.76 eV of $BiVO_4$ and 0.80 and 3.38 eV of WO_3, respectively, which were calculated from the Equation (2.3) in Chapter 2 with χ and E_g of 6.04 eV [36] and 2.45 eV for $BiVO_4$ and 6.59 eV [42] and 2.58 eV for WO_3, respectively. These results were in good agreement with the previous reports [36, 42].

As shown in Figure 4.23, MB can be activated by the visible light irradiation to generate the MB* and inject electron to CB of $BiVO_4$ [37]. Simultaneously, $BiVO_4$ and WO_3 particles can also absorb the visible light and generate electron and hole pairs. When the $BiVO_4/WO_3$ composite is irradiated with visible light, photoexited electrons can be generated in the CB of the $BiVO_4$, which can be inject to the CB of WO_3 easily due to the potential difference. Alternatively, photogenerated holes in the VB of WO_3 can transfer to the VB of $BiVO_4$. The potential at VB of $BiVO_4$ will then react with the adsorbed water molecules on their surface to produce hydroxyl radicals, and the adsorbed MB molecules can be oxidized by theses hydroxyl radicals [36, 37, 42].

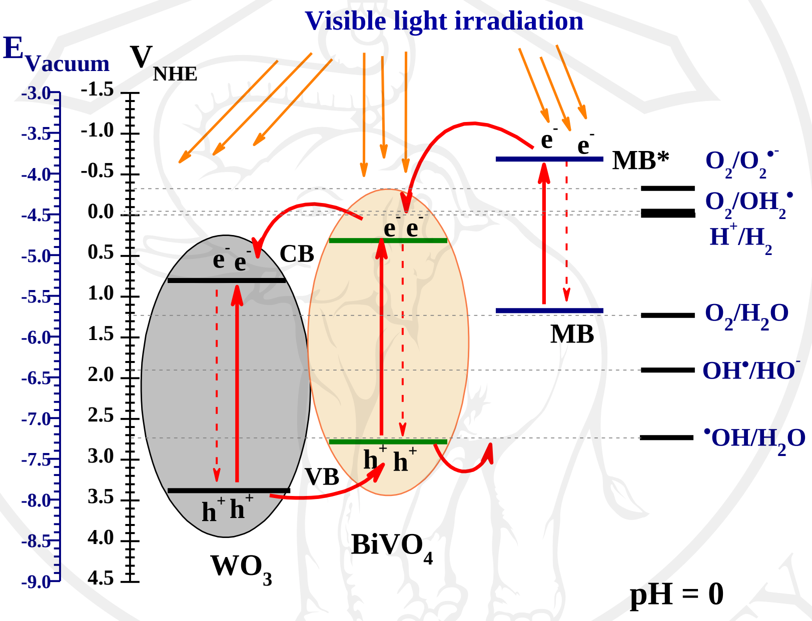

Figure 4.23 Schematic diagram of charge separation of $BiVO_4/WO_3$ heterostructure photocatalysts under visible light irradiation at pH 0.

For applying to practical applications, the stability of photocatalysts is the important point to study. In this research, the stability and recyclability of the 4:1$BiVO_4/WO_3$ composite film for degradation of MB dye was studied with the same experimental conditions during each run the film was annealed at 250°C for 1 h to remove the organic contaminants from the surface of catalyst film. Figure 4.24 shows the 4:1$BiVO_4/WO_3$ composite film was reused five times. It was found that after five recycles the photocatalytic activity had no significant changes for the photodegradation of MB over of the catalyst film under visible light irradiation.

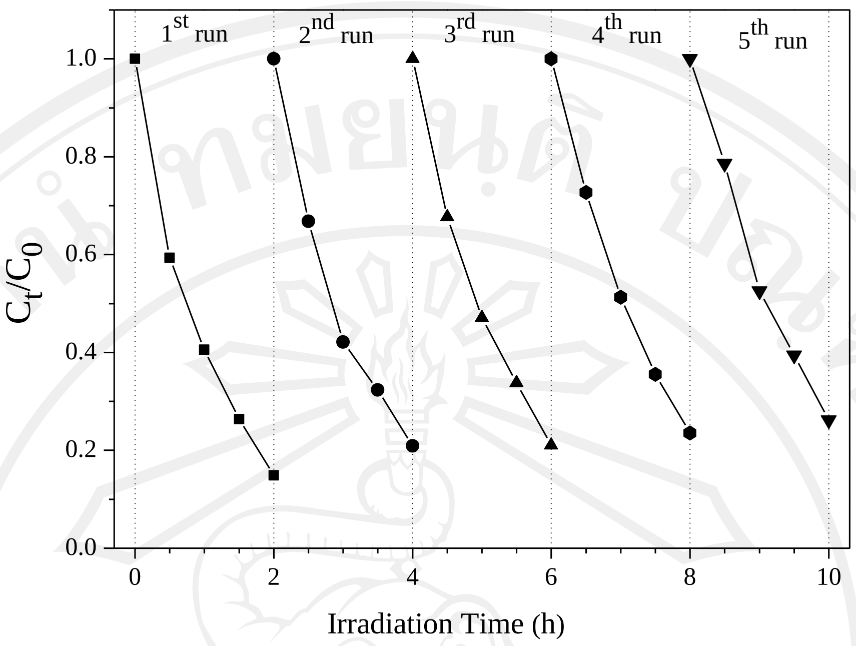

Figure 4.24 Recycling runs of methylene blue solution in the photodegradation on 4:1$BiVO_4/WO_3$ photocatalytic film.

4.5 Comparative photocatalytic activity of $BiVO_4/CeO_2$, $BiVO_4/TiO_2$ and $BiVO_4/WO_3$ composites

Considerations of coupling between two semiconductors with different appropriate energy levels of $BiVO_4/WO_3$, $BiVO_4/TiO_2$ and $BiVO_4/CeO_2$ at pH 0 are presented in Figure 4.25, which corresponded to photocatalytic activities for MB degradation that of the $BiVO_4/CeO_2$ composite exhibited higher than those of the $BiVO_4/TiO_2$ and $BiVO_4/WO_3$ composites. These can be described that the mechanisms of the three different composites as follows:

When the coupled $BiVO_4/CeO_2$ is irradiated with visible light, $BiVO_4$ and CeO_2 in the composite can be activated. Since $BiVO_4$ has the CB and VB potential edges more positive than CeO_2 (Figure 4.25), the excited electrons in CB of CeO_2 can be injected to the CB of $BiVO_4$, whereas the photogenerated holes at the VB of $BiVO_4$ can be transferred the VB of CeO_2. The adsorbed oxygen molecules on the surface of the CeO_2 can be reduced by electrons at its CB to generate finally hydroxyl radicals,and the absorbed water molecules on the surface of the $BiVO_4$ can be oxidized by potential at its

VB to produce hydroxyl radicals. Thus, there are two main mechanisms of the $BiVO_4/CeO_2$ composite to degrade MB, which favour to adsorb on the surface of a high negative surface charge of $BiVO_4$ at pH 7 (Figure 4.26), leading this composites showed the highest photocatalytic activity for degradation of MB.

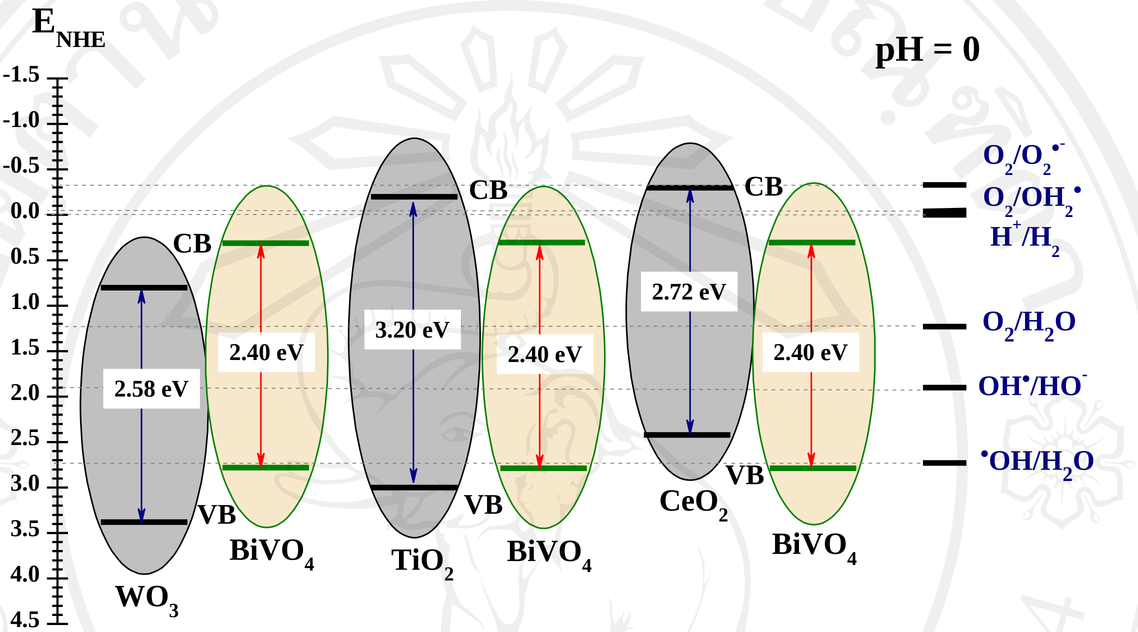

Figure 4.25 The possible band edge positions of coupled $BiVO_4/WO_3$, $BiVO_4/TiO_2$ and $BiVO_4/CeO_2$ at pH 0.

For $BiVO_4/TiO_2$ composite, the CB and VB of $BiVO_4$ are located between the CB and VB of TiO_2, in which the band gap energy of $BiVO_4$ (2.4 eV) is smaller than TiO_2 (3.2 eV). Under visible light irradiation, MB molecule in aqueous solution can adsorb the visible light to generate the MB* and inject electron to CB of TiO_2. The electron from the more negative CB of TiO_2 can reduce surface chemisorbed O_2 to $O_2^{\bullet -}$, which showed the main mechanism of this system. According to the TiO_2 nanoparticles covered on the surface of $BiVO_4$ particles, and also TiO_2 provided high surface area with negatively surface charge at pH 7 (Figure 4.26) which MB molecules favour to adsorb on the TiO_2 surface. Thus, the $BiVO_4/TiO_2$ composite showed lower photocatalytic activity than that of $BiVO_4/CeO_2$ composite.

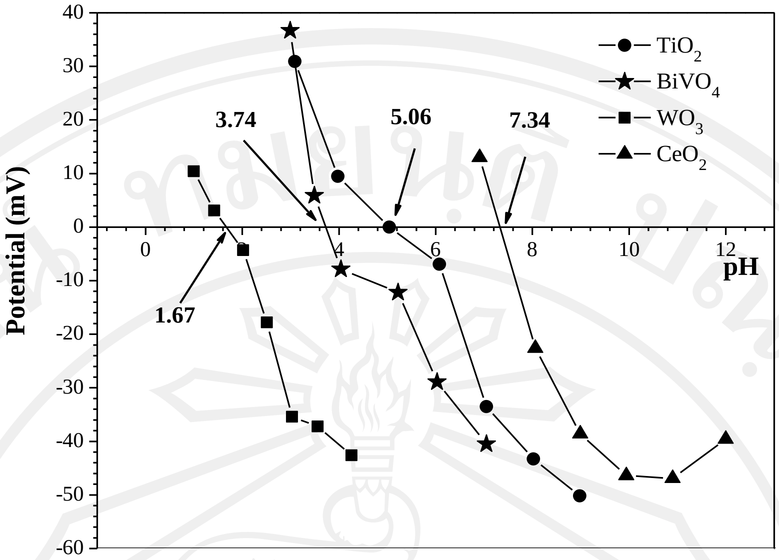

Figure 4.26 pH dependence of zeta potential of the $BiVO_4$, TiO_2, WO_3 and CeO_2 in an aqueous solution.

In the $BiVO_4/WO_3$ composite, the CB and VB potential edges of $BiVO_4$ are more negative than those of WO_3, which is the opposite configuration to the $BiVO_4/CeO_2$ composite. The $BiVO_4$ and WO_3 can be activated by visible light irradiation and generated electron and hole pairs. The electrons at the CB of $BiVO_4$ then transfer to the CB of WO_3, but they cannot reduce absorbed O_2 to radical species due to both CB potentials are more positive than redox potential of reduction of O_2 to $O_2^{-\bullet}$ and $OH_2^{\bullet}$. On the other hand, the photogenerated holes at the VB of WO_3 can transfer to the CB of $BiVO_4$, which can oxidize H_2O to $OH^{\bullet}$. It is found that only one mechanism in this composite system at VB of $BiVO_4$ produce the hydroxyl radicals for degrading MB but they preferably adsorb on the surface of WO_3 than $BiVO_4$. As in Figure 4.21, WO_3 film showed highest adsorptive efficiency with corresponding to zeta potential data in Figure 4.26. Therefore, the $BiVO_4/WO_3$ composite exhibited the lowest photocatalytic activity as compared to the $BiVO_4/CeO_2$ and $BiVO_4/TiO_2$ composites.

4.6 Conclusions

$BiVO_4/TiO_2$ composite powders with mole ratios of 4:1, 3:2, 1:1, 2:3 and 1:4 were successfully synthesized by a coupling of the precipitation and sol-gel methods. Based on the characterization results of XRD, Raman, XPS, TEM, UV-vis DRS and N_2 adsorption-desorption, the influence of coupling $BiVO_4$ with TiO_2 on the crystal phase, morphology, band structure, surface element composition, morphology, optical absorption and surface area of the synthesized composites were investigated. The results showed that the high surface area of the composites, which composed of the minor phase of anatanse TiO_2 nanoparticles attached on the surface of the major phase of monoclinic $BiVO_4$ particles to form the heterostructure with the chemical interaction. The synthesized $BiVO_4/TiO_2$ composite powders were also fabricated on glass substrates used for photodegradation of MB dye under visible light irradiation, and all the as-prepared composite films exhibited the enhanced photocatalytic activities, which the composite film with mole ratio of 1:1 exhibited the highest photocatalytic activity. Their enhanced photocatalytic activities could be attributed to the transfer of electron, and the separation of electrons and holes was efficiently improved, which could be favorable for the enhancement of photocatalytic activity. It was also found that the photocatalytic reaction followed the pseudo first order kinetic model in the presence of all synthesized photocatalyst. The possible mechanism of reduction process at the CB of TiO_2 produced oxidizing radicals for degradation of MB under visible light irradiation.

$BiVO_4/WO_3$ composites with different ratios were successfully synthesized by a co-precipitation method, and characterized by XRD Raman, XPS, TEM, UV-vis DRS and N_2 adsorption-desorption. XRD and Raman analyses revealed that the two phases were composed of the monoclinic $BiVO_4$ and monoclinic WO_3. The XPS and TEM results confirmed that the formation of WO_3 particles attracted $BiVO_4$ particles of the $BiVO_4/WO_3$ composites with chemical interactions. The specific surface areas increased with increasing mole ratio of WO_3, which could enhance their photocatalytic activity. On the other hand, the photocatalytic activities of the $BiVO_4/WO_3$ composites increased, when the absorption edges of $BiVO_4/WO_3$ composites showed more red shift to visible region with increasing the mole ratio of $BiVO_4$. Thus, the $BiVO_4/WO_3$ composites displayed much higher photocatalytic activities on the degradation of than the pure WO_3 under visible light irradiation, and the $BiVO_4/WO_3$ molar ratio of 4:1 showed the highest photocatalytic activity for degradation of MB. In this system of the $BiVO_4/WO_3$ composite, the main reaction for photocatalytic activity was oxidation process at the VB of $BiVO_4$, which generated active radicals to degrade MB.

4.7 References

[1] Kudo A. Photocatalyst materials for water splitting, *Catal. Surv. Asia*, 2003, **7**, 31–38.

[2] Bhatkhande D.S., Pangarkar V.G., Beenackers A.C.M. Photocatalytic degradation for environmental applications - a review, *J. Chem. Technol. Biotechnol.*, 2002,**77**, 102–116.

[3] Wang D.E., Li R.G., Zhu J., Shi J.Y., Han J.F., Zong X. Photocatalytic water oxidation on $BiVO_4$ with the electrocatalyst as an oxidation cocatalyst: Essential relations between electrocatalyst and photocatalyst, *J. Phys. Chem. C*, 2012, **116**, 5082–5089.

[4] Pelaez M., Nolan N.T., Pillai S.C., Seery M.K., Falaras P., Kontos A.G. A review on the visible light active titanium dioxide photocatalysts for environmental applications, *Appl. Catal. B*, 2012, **125**, 331–349.

[5] Feng H., Zhang M.H., Yu L.E. Hydrothermal synthesis and photocatalytic performance of metal-ions doped TiO_2, *Appl. Catal. A*, 2012, **413–414**, 238–44.

[6] Chatchai P., Murakami Y., Kishioka S., Nosaka A.Y, Nosaka Y. Efficient photocatalytic activity of water oxidation over $WO_3/BiVO_4$ composite under visible light irradiation, *Electrochim. Acta*, 2009, **54**, 1147–1152.

[7] Gupta S., Tripathi M. A review of TiO_2 nanoparticles, *Chinese Sci. Bull.*, 2011, **56**, 1639–57.

[8] Ahmed S., Rasul M.G., Martens W.N., Brown R., Hashib M.A. Heterogeneous photocatalytic degradation of phenols in wastewater: A review on current status and developments, *Desalination*, 2010, **261**, 3–18.

[9] Li L., Yan B. $BiVO_4/Bi_2O_3$ submicrometer sphere composite: Microstructure and photocatalytic activity under visible-light irradiation, *J. Alloy. Compd.*, 2009, 476, 624–628.

[10] Chen L., Zhang Q., Huang R., Yin S.F., Luo S.L., Au C.T. Porous peanut-like Bi_2O_3-$BiVO_4$ composites with heterojunctions: One-step synthesis and their photocatalytic properties, *Dalton Trans.*, 2012, **41**, 9513–9518.

[11] Jiang H.Q., Nagai M., Kobayashi K. Enhanced photocatalytic activity for degradation of methylene blue over $V_2O_5/BiVO_4$ composite, *J. Alloy. Compd.*, 2009, **479**, 821–827.

[12] Su J., Zou X.X., Li G.D., Wei X., Yan C., Wang Y.N. Macroporous V_2O_5-$BiVO_4$ composites: Effect of heterojunction on the behavior of photogenerated charges. *J. Phys. Chem. C*, 2011, **115**, 8064–8071.

[13] Ji T.H., Yang F., Zhou J.Y., Du H.Y., Sun J.Y. Visible-light responding $BiVO_4/TiO_2$ nanocomposite photocatalyst, *Spectros. Spect. Analys.*, 2010, **30**, 1944–1947.

[14] Hu Y., Li D., Zheng Y., Chen W., He Y., Shao Y. $BiVO_4/TiO_2$ nanocrystalline heterostructure: A wide spectrum responsive photocatalyst towards the highly efficient decomposition of gaseous benzene, *Appl. Catal. B*, 2011, **104**, 30–36.

[15] Zhang L., Tan G., Wei S., Ren H., Xia A., Luo Y. Microwave hydrothermal synthesis and photocatalytic properties of $TiO_2/BiVO_4$ composite photocatalysts, *Ceram. Int.*, 2013, **39**(8), 8597–8604

[16] Chatchai P., Nosaka A.Y., Nosaka Y. Photoelectrocatalytic performance of $WO_3/BiVO_4$ toward the dye degradation, *Electrochim. Acta*, 2013, **94**, 314–319.

[17] Hong S.J., Lee S., Jang J.S., Lee J.S. Heterojunction $BiVO_4/WO_3$ electrodes for enhanced photoactivity of water oxidation, *Energy Environ. Sci.*, 2011, **4**, 1781–1787.

[18] Su J., Guo L., Bao N., Grimes C.A. Nanostructured $WO_3/BiVO_4$ heterojunction films for efficient photoelectrochemical water splitting, *Nano Lett.*, 2011, **11**, 1928–1933.

[19] Jiang J, Wang M, Li R, Ma L, Guo L. Fabricating $CdS/BiVO_4$ and $BiVO_4/CdS$ heterostructured film photoelectrodes for photoelectrochemical applications, *Int. J. Hydrogen Energ.*, 2013, **38**, 13069–13076.

[20] Bajaj R., Sharma M., Bahadur D. Visible light-driven novel nanocomposite ($BiVO_4/CuCr_2O_4$) for efficient degradation of organic dye, *Dalton Trans.*, 2013, **42**, 6736–6744.

[21] Pilli S.K., Deutsch T.G., Furtak T.E., Brown L.D., Turner J.A., Herring A.M. $BiVO_4/CuWO_4$ heterojunction photoanodes for efficient solar driven water oxidation, *Phys. Chem. Chem. Phys.*, 2013, **15**, 3273–3278.

[22] Yu J., Zhang Y., Kudo A. Synthesis and photocatalytic performances of $BiVO_4$ by ammonia co-precipitation process, *J. Solid State Chem.*, 2009, **182**, 223–228.

[23] Wetchakun N., Incessungvorn B., Wetchakun K., Phanichphant S. Influence of calcination temperature on anatase to rutile phase transformation in TiO_2 nanoparticles synthesized by the modified sol–gel method, *Mater. Lett.*, 2012, **82**, 195–198.

[24] Wetchakun N., Chaiwichain S., Inceesungvorn B., Pingmuang K., Phanichphant S., Minett A.I., Chen J. $BiVO_4/CeO_2$ Nanocomposites with high visible-light-induced photocatalytic activity, *ACS Appl. Mater. Interfaces*, 2012, **4**, 3718–3723.

[25] Nattestad A., Ferguson M., Kerr R., Cheng Y.B., Bach U. Dye-sensitized nickel(II)oxide photocathodes for tandem solar cell applications, *Nanotechnology*, 2008, **19**, 295304.

[26] Miao L., Tanemura S., Toh S., Kaneko K., Tanemura M. Fabrication, characterization and Raman study of anatase-TiO_2 nanorods by a heating sol-gel template process, *J. Cryst. Growth*, 2004, **264**, 246–252.

[27] Xue X., Ji W., Mao Z., Mao H., Wang Y., Wang X. Raman investigation of nanosized TiO_2: Effect of crystallite size and quantum confinement, *J. Phys. Chem. C*, 2012, **116**, 8792–8797.

[28] Gotić M., Musić S., Ivanda M., Šoufek M., Popović S. Synthesis and characterisation of bismuth(III) vanadate, *J. Mol. Struct.*, 2005, **744–747**, 535–540.

[29] Zhang A., Zhang J., Cui N., Tie X., An Y., Li L. Effects of pH on hydrothermal synthesis and characterization of visible-light-driven $BiVO_4$ photocatalyst, *J. Mol. Catal. A*, 2009, 304, 28–32.

[30] Xiaodan Y., Qingyin W., Shicheng J., Yihang G. Nanoscale ZnS/TiO_2 composites: Preparation, characterization, and visible-light photocatalytic activity, *Mater. Charact.*, 2006, **57**, 333–341.

[31] Obregon S., Colon G. A ternary Er^{3+}-$BiVO_4$/TiO_2 complex heterostructure with excellent photocatalytic performance. *RSC Advances*, 2014, 4, 6920–6926.

[32] Uddin M.T., Nicolas Y., Olivier C., Toupance T., Müller M.M., Kleebe H.J. Preparation of RuO_2/TiO_2 mesoporous heterostructures and rationalization of their enhanced photocatalytic properties by band alignment investigations, *J. Phys. Chem. C*, 2013, **117**, 22098–22110.

[33] Kim C., Kim K.S., Kim H.Y., Han Y.S. Modification of a TiO_2 photoanode by using Cr-doped TiO_2 with an influence on the photovoltaic efficiency of a dye-sensitized solar cell, *J. Mater. Chem.*, 2008, **18**, 5809–5814.

[34] Nethercot A.H. Prediction of fermi energies and photoelectric thresholds based on electronegativity concepts, *Phys. Rev. Lett.*, 1974, **33**, 1088–1091.

[35] Tian J., Sang Y., Zhao Z., Zhou W., Wang D., Kang X. Enhanced photocatalytic performances of CeO_2/TiO_2 nanobelt heterostructures, *Small*, 2013, **9**, 3864–3872.

[36] Jiang H., Endo H., Natori H., Nagai M., Kobayashi K. Fabrication and efficient photocatalytic degradation of methylene blue over $CuO/BiVO_4$ composite under visible-light irradiation, *Mater. Res. Bull.,* 2009, **44**,700–706.

[37] Seema H., Kemp K.C., Chandra V., Kim K.S. Graphene-SnO_2 composites for highly efficient photocatalytic degradation of methylene blue under sunlight, *Nanotechnology,* 2012, **23**, 355705.

[38] Kohtani S., Yoshida K., Maekawa T., Iwase A., Kudo A., Miyabe H. Loading effects of silver oxides upon generation of reactive oxygen species in semiconductor photocatalysis, *Phys. Chem. Chem. Phys.*, 2008, **10**, 2986–2992.

[39] Djaoued Y., Balaji S., Beaudoin N. Erratum to: Sol-gel synthesis of mesoporous WO_3-TiO_2 composite thin films for photochromic devices. *J. Sol-Gel Sci. Technol.,* 2013, **68**, 516–525.

[40] Leghari S.A.K., Sajjad S., Chen F., Zhang J. WO_3/TiO_2 composite with morphology change via hydrothermal template-free route as an efficient visible light photocatalyst, *Chem. Eng. J.*, 2011, **166**, 906–915.

[41] Zhang S., Li H., Zhong Q. Promotional effect of F-doped V_2O_5-WO_3/TiO_2 catalyst for NH_3-SCR of NO at low-temperature, *Appl. Catal. A,* 2012, **435–436**, 156–162.

[42] Shifu C., Lei J., Wenming T., Xianliang F. Fabrication, characterization and mechanism of a novel Z-scheme photocatalyst $NaNbO_3/WO_3$ with enhanced photocatalytic activity, *Dalton Trans.,* 2013, **42**, 10759–10768.